

The Halos and Environments of Nearby Galaxies (HERON) I: Imaging, Sample Characteristics, and Envelope Diameters

R. Michael Rich,^{1*} Aleksandr Mosenkov,² Henry Lee-Saunders,¹ Andreas Koch,³ John Kormendy,⁴ Julia Kennefick,⁵ Noah Brosch,⁶ Laura Sales,⁷ James Bullock,⁸ Andreas Burkert,⁹ Michelle Collins,¹⁰ Michael Cooper,⁸ Michael Fusco,⁵ David Reitzel,¹¹ David Thilker,¹³ Dave G. Milewski,¹⁴ ¹⁶ Lydia Elias,⁷ M. L. Saade,¹ and Laura De Groot¹⁵

¹*Department of Physics & Astronomy, Univ. of California Los Angeles, 430 Portola Plaza, Los Angeles, CA 90095-1547, USA*

²*Central Astronomical Observatory, Russian Academy of Sciences, 65/1 Pulkovskoye chaussee, St. Petersburg, 196140 Russia*

³*Zentrum für Astronomie der Universität Heidelberg, Astronomisches Rechen-Institut, 69120 Heidelberg, Germany*

⁴*Department of Astronomy, Univ. of Texas at Austin, 2515 Speedway, Mail Stop C1400, Austin, TX 78712-1205, USA*

⁵*Department of Physics, Univ. of Arkansas, 825 West Dickson Street, Fayetteville, AR 72701, USA*

⁶*Wise Observatory, Tel Aviv University, 69978 Tel Aviv, Israel*

⁷*Department of Physics & Astronomy, Univ. of California Riverside, Riverside 92521, CA, USA*

⁸*Department of Physics & Astronomy, Univ. of California, Irvine, 4129 Frederick Reines Hall, Irvine 92697-4575, CA, USA*

⁹*Department of Physics, Ludwig-Maximilians Universität München, Schellingstrasse 4, 80799 Munich, Germany*

¹⁰*Department of Physics, Univ. of Surrey, Surrey GU2 7XH, United Kingdom*

¹¹*Griffith Observatory, 2800 East Observatory Road, Los Angeles 90027, CA, USA*

¹³*Department of Physics and Astronomy, Johns Hopkins University, 3400 N. Charles Street, Baltimore, MD 21218, USA*

¹⁴*Department of Earth, Planetary, & Space Sciences, 595 Charles Young Drive, Univ. of California Los Angeles, CA 90095-1567, USA*

¹⁵*Department of Physics, The College of Wooster, 308 E. University Street, Wooster, OH 44691, USA*

¹⁶*NASA Jet Propulsion Laboratory, 4800 Oak Grove Drive, Pasadena, CA 91109-8001, USA*

Accepted XXX. Received YYY; in original form ZZZ

ABSTRACT

We use a dedicated 0.7-m telescope to image the halos of 119 galaxies in the Local Volume to $\mu_r \sim 28 - 30$ mag/arcsec². The sample is primarily from the 2MASS Large Galaxy Atlas and extended to include nearby dwarf galaxies and more distant giant ellipticals, and spans fully the galaxy colour–magnitude diagram including the blue cloud and red sequence. We present an initial overview, including deep images of our galaxies. Our observations reproduce previously reported low surface brightness structures, including extended plumes in M 51, and a newly discovered tidally extended dwarf galaxy in NGC 7331. Low surface brightness structures, or “envelopes”, exceeding 50 kpc in diameter are found mostly in galaxies with $M_V < -20.5$, and classic interaction signatures are infrequent. Defining a halo diameter at the surface brightness 28 mag/arcsec², we find that halo diameter is correlated with total galaxy luminosity. Extended signatures of interaction are found throughout the galaxy colour–magnitude diagram without preference for the red or blue sequences, or the green valley. Large envelopes may be found throughout the colour–magnitude diagram with some preference for the bright end of the red sequence. Spiral and S0 galaxies have broadly similar sizes, but ellipticals extend to notably greater diameters, reaching 150 kpc. We propose that the extended envelopes of disk galaxies are dominated by an extension of the disk population rather than by a classical population II halo.

Key words: Galaxies: evolution - formation - halos - interactions - photometry - structure

* E-mail: rmr@astro.ucla.edu

1 INTRODUCTION

The stellar outskirts or envelopes of galaxies are frequently described using the term “halo”, even though their component stellar populations are unlikely to resemble the Population II stellar population normally associated with the Milky Way halo. These envelopes may range from classical old Population II stars to accreted low luminosity galaxies that may still host star formation and gas. The situation is further complicated by evidence that galactic halos consist of a mixture of accreted (outer) and in-situ (inner) components (e.g. Cooper et al. 2013; Pillepich et al. 2015), or metal rich stars related to the spheroid (e.g. Bellazzini et al. 2003). As such, these extended stellar envelopes might consist of ancient halo stars formed in-situ, debris from an ingested galaxy, relics of stages in the formation of the disk, or stars ejected from the disk of the host galaxy experiencing accretion.

By way of example, deep *Hubble Space Telescope* (*HST*) imaging on the minor axis of M 31 (Brown et al. 2003; Brown et al. 2006) revealed a substantial intermediate-age population. The halo of M 31 is mostly metal rich (Rich et al. 1996; Durrell et al. 2001; Bellazzini et al. 2003) while also hosting both globular clusters, RR Lyrae stars, and a host of substructures in the form of satellites and streams (e.g. McConnachie et al. 2009). Simulations like those of e.g. Mori & Rich (2008) show that a minor merger with a galaxy of mass $M \sim 10^9 M_\odot$ can reproduce the many complex structures similar to those seen in the M 31 halo as well as ejecting stars from the disk.

Ideally, this study would separate out the different populations of halo stars (in-situ, accreted, and disturbed disk) using the colours and magnitudes of the stars. However, the age–metallicity degeneracy that affects interpretation of colours and spectra also would affect the stars in the resolved stellar population. As the origins of these structures might be so varied, we must use the term “halos” to mean a more complicated type of stellar population than the conventional e.g. Population II. Recent extensive surveys of interaction signatures of galaxies bear this out; studies by Atkinson et al. (2013), Hood et al. (2018), and Morales, Martínez-Delgado, Grebel, Cooper, Javanmardi & Miskolczi (2018) report a wide variety of interaction signatures across the galaxy color–magnitude diagram. These range from organized shells observed around luminous red galaxies, to a huge array of disturbances associated with disks. An examination of the range of interactions raises the question of what the extended structures of galaxies are comprised of, likely a mix of debris from the host and the merger galaxy. For the purposes of our investigation, these low surface brightness structures will be referred to as envelopes, as the term “halo” might imply a more specific stellar population.

Studies have also shown that the type of envelope a galaxy possesses may relate to its mass. A small survey of galaxy envelope fields from photometric metallicities of resolved stars imaged using *HST* finds an interesting dichotomy, in which galaxies with $M_V < -21$ have relatively metal rich envelopes (e.g. $[Fe/H] = -0.7$) and lower luminosity envelopes have lower metallicity, closer to -1.5 dex. (Mouhcine et al. (2005); Monachesi et al. (2016); Harmsen et al. (2017)). Although this kind of investigation requires more development, it is important to reflect that more lumi-

nous galaxies may have envelopes more related to their central bulges and spheroids, while disk galaxies lacking bulges (e.g. NGC 4244) have a more metal-poor envelope. The field of low surface brightness imaging has recently been associated with the discovery of shell structures around elliptical galaxies, spectacular interaction streams, and a zoo of peculiar extensions and structures (e.g. Martínez-Delgado et al. 2010; Duc 2017). Relatively less attention has been paid to investigating the systematics of the quotidian envelopes extending to low surface brightness surrounding galaxies, that represent the potentially very long-lived structures. Our investigation explores the correlation of this relaxed envelope diameter with galaxy absolute magnitude, and in this initial study, we explore how envelope diameter varies across the galaxy colour–magnitude diagram.

This paper formally introduces the *HERON* project, an international collaboration of observers and theorists working to motivate observations of the low surface brightness extensions of galaxies and to compare those results with theory. Future papers will report analysis of quantitative surface brightness profiles, outer envelope morphologies, and other properties including comparisons of extended structures to imaging data at other wavelengths. We will also publish catalogues and luminosities for all low surface brightness candidate companions in the survey. In this project, we build on the heritage of Kormendy & Bahcall (1974) and report envelope diameters to 28 mag/arcsec^2 for 119 galaxies. Starting in 2019 October, we will begin populating the *HERON* archive at IRSA/IPAC in the community data archives;¹ we will provide data tables, JPEG, and FITS images for the full galaxy sample in the *HERON* survey.

This paper is organized as follows: Sect. 2 presents our instrumentation, observing strategy, and data reduction. The sample of *HERON* galaxies is introduced in Sect. 3, along with the measurement of their envelope diameters. In Sect. 4 we discuss our results, while in Sect. 5 we correlate our results with general galaxy properties, before summarizing in Sect. 6.

1.1 A brief history of low-surface brightness features

The study of low surface brightness galaxy envelopes and extensions has a long history with many interesting subjects; Zwicky (1956) used apertures from the 18-inch Schmidt to the Hale 200-inch telescope, and called attention to tidal tails and extensions of galaxies including NGC 3628. He also emphasized the value of studying such systems by noting the much earlier works of, e.g., Pease (1920) and Lundmark (1920). Other early contributions include the career-long work of Karachentsev (1965), which continues to the present day (Karachentsev et al. 2017). Photoelectric photometry exploring the extent of M 87 to a full degree (De Vaucouleurs 1969; Arp & Bertola 1969) was also a remarkably early application of technology to the problem. The analysis of scanned photographic plates of Kormendy & Bahcall (1974) was the first to report a photographic image of the giant stream of NGC 3628, and to report the diameter measurements for a large number of envelopes, some as large as 100 kpc.

¹ www.irsa.ipac.caltech.edu/data/HERON/

Low surface brightness studies returned to the spotlight with the pioneering work of e.g. Malin (1978), Malin (1979), and Malin & Carter (1980). Malin & Hadley (1997) illustrate the remarkable low surface brightness envelopes and streams of spiral galaxies, including a giant arc near M 83. These efforts included the development of ‘unsharp masking’ and the discovery of low surface brightness shells around elliptical galaxies. Binggeli et al. (1988) catalogued the Virgo cluster including dwarf galaxies, continued by Ferguson & Sandage (1989). The subject has seen contemporary vitality with the now decades-old explosion of modest aperture telescopes with CCD detectors that have revealed surprisingly extended envelopes of nearby galaxies (e.g. Tal et al. 2009; Martínez-Delgado et al. 2010; Rich et al. 2012; Martínez-Delgado et al. 2012; Van Dokkum et al. 2015; Trujillo & Fliri 2016) and significant work using the Burrell Schmidt Telescope (Mihos et al. 2005; Watkins et al. 2015; Mihos et al. 2017). Duc et al. (2015) undertook low surface brightness imaging of the environs of ATLAS3D ² ellipticals, updating the Tal et al. (2009) sample, and finding numerous cases of streams, shells, and extended disk star formation. The Pan-Andromeda Archaeological Survey (PanDAS) map of the resolved stellar halo of the nearby Andromeda-M 33 complex reveals significant halo structures, demonstrating that the entire extent of the M 31 envelope may stretch halfway to the Milky Way and significantly overlaps with that of the neighbouring spiral M 33 (McConnachie et al. 2009; Ibata et al. 2013; see also Koch et al. 2008). The interesting science questions raised by these analyses have inspired a range of investigations that include networks of small telescopes (Martínez-Delgado et al. 2012), an array of 8 (now 2×24) Canon telephoto camera lenses (the Dragonfly project; Abraham & Van Dokkum 2014; Van Dokkum et al. 2014; Merritt et al. 2016) and our project – the *Halos and Environments of Nearby Galaxies (HERON)* survey Rich et al. 2017.

Any new entry into this subject area faces the long history of research and also serious challenges such as the correct treatment of scattered light (Sandin 2014, 2015). Furthermore, the instrumentation required to enter the field, for the most part, is modest in cost, enabling numerous individuals and teams to participate. A successful philosophy has been to aggregate very long exposures obtained by citizen scientists with state of the art, commercial off the shelf equipment (e.g. Martínez-Delgado et al. 2010). The Dragonfly array employs commercial technology to minimize scattered light, and builds a powerful instrument from multiple focal planes. An additional relatively recent project is the Purple Mountain 1.0 -m Schmidt Near Earth Object Survey Telescope (Shi et al. 2017); this facility has been used to investigate ultra-diffuse galaxies. Special purpose telescopes are under construction and a small space mission has been proposed to undertake imaging at low surface brightness (Muslimov et al. 2017). Serendipitous imaging of galaxy outskirts into resolved stars will also occur as part of the WFIRST mission. In fact, the systematics of Galactic cirrus and scattered light probably, in all likelihood, limit quantitative investigations to the 30–32 mag/arcsec² (in the *r* band) level (for an extreme case of the effects of infrared

cirrus, as e.g. for NGC 7743). Pushing fainter than this will require space-based mission that is capable of resolving the low surface brightness structures into stars.

1.2 Theoretical motivation

The low-surface brightness envelopes of nearby galaxies offer a unique window into galaxy formation and evolution, and possibly cosmology. These regions hold clues to the hierarchical build-up of structure formation on sub-galactic scales, the very scales where the dominant Λ CDM paradigm is facing its most difficult challenges. Some of the most profound concerns about the Λ CDM theory have arisen in comparison to dwarf satellites and low-surface brightness features seen around just two galaxies: the Milky Way and M 31 (Boylan-Kolchin et al. 2011, 2012). But by relying on just two galaxies of similar luminosity and type we are potentially biasing ourselves significantly. Despite its marked successes in reproducing the large-scale properties of the Universe, the Λ CDM cosmological model faces some significant problems on the mass scales of dwarf galaxies ($M_* \sim M_{vir} = 10^{5-9} M_\odot$). The overall count of dwarfs throughout the Local Group is significantly lower than might naively be expected in Λ CDM-based models of galaxy formation (the “missing satellites” problem; Klypin et al. 1999; Moore et al. 1999). Moreover, the measured internal mass densities of dwarf satellites are significantly lower than predicted for the ~ 10 most massive dark matter halos near galaxies similar to the Milky Way (the “too big to fail” problem; Boylan-Kolchin et al. 2011, 2012; Agertz & Kravtsov 2016).

These anomalies do not necessarily mean that our cosmology needs to be revised, as plausible astrophysical solutions have been proposed (e.g. Bullock et al. 2000; Governato et al. 2010; Di Cintio et al. 2014; Wetzel et al. 2016), but they do strongly motivate the need for alternative tests of the paradigm on the mass scales of dwarf galaxies. One particularly robust test involves looking for tell-tale signs of past dwarf-size merger events around local galaxies: low-surface brightness streams, diffuse halo light, and faint heated disk material (Johnston 1998; Bullock et al. 2001, Bullock & Johnston 2005; Kazantzidis et al. 2008; Purcell et al. 2010; Cooper et al. 2010; Amorisco 2017). While theoretically well motivated, searches of this kind have been limited largely to resolved-star studies around the Milky Way and M 31 (McConnachie et al. 2009; Belokurov et al. 2006; Belokurov et al. 2007; Bechtol et al. 2015; Cunningham et al. 2016; Mackey et al. 2016). The reason is that the predicted features are extremely low surface brightness, $\sim 29 - 30$ mag/arcsec². Until recently, faint features of this kind were prohibitively difficult to detect without resolving them into stars.

Why are low-surface brightness features so important? Primarily because the predictions are robust: they rely on the assumption that structure formation is hierarchical down to small scales – one of the fundamental predictions of cold dark matter cosmologies. More specifically, if Λ CDM is correct, then galaxy-size dark matter halos should be built by the steady accretion of smaller, dwarf-size dark matter clumps (e.g. Cole et al. 2000; Stewart et al. 2008; Fakhouri et al. 2010). The rate and timing of these dark-matter halo mergers are robustly predicted, at least statistically speaking. Moreover, the stellar content of these dark matter mergers is also well constrained, as the stellar mass of dwarf

² www-astro.physics.ox.ac.uk/atlas3d/

galaxies needs to drop steeply with decreasing halo mass in a well-defined way to solve the missing satellites problem and (more generally) to explain the observed faint-end of the luminosity function (e.g. Behroozi et al. 2013; Garrison-Kimmel et al. 2017; Read et al. 2017, loosely called “abundance matching”).

The implication is that it should be relatively straightforward to predict the fraction of a galaxy’s light contained in diffuse, low-surface brightness material as a function of galaxy stellar mass. Purcell et al. (2010) made this point explicitly using a semi-analytic model, and showed that the diffuse light fraction (stellar halo light fraction) should vary strongly with galaxy mass over the galaxy scales of interest here.

2 OBSERVATIONS AND DATA REDUCTION

Our approach to the *HERON* project has been to use and maintain two dedicated telescopes that are proven to reach low levels of surface brightness rapidly, allowing us to upgrade the focal planes, and experiment with different filters and observing modes, all at reasonable cost.

2.1 Instrumentation

We employ the 0.7-m Jeanne Rich Telescope Centurion 28 (C28) at the Polaris Observatory Association site, a dedicated f/3.2 telescope with a prime focus imager behind a Ross doublet corrector, consisting of FS2 and BK7 glass. A conical baffle with ring stops is placed in front of the corrector group to control scattered light. The primary mirror is honeycomb light weighted, and the truss consists of graphite epoxy rods in tension; the optical telescope assembly is supported on an equatorial yoke mount. The control system employs the FS2 astro-electronic telescope control system, by Michael Koch³. Focus is achieved using a motor by Robofocus, which focuses by moving the corrector group. The telescope is illustrated in Brosch (2015a) and Rich et al. (2017).

The observatory is located in Lockwood Valley, near Frazier Park, CA at an elevation of 1615 m. Although the greater Los Angeles area creates a light dome in the Southeast, the site is 21.7 – 22.0 mag/arcsec² at the zenith and very dark in the West. The manufacturer, James Riffle of AstroWorks Corp in Arizona, produced a number of 0.5-m telescopes of similar design (Brosch et al. 2008) and an identical telescope (the 0.7-m Jay Baum Rich Telescope) operates at Wise Observatory, Israel near Mitzpe Ramon (Brosch 2015a; Brosch et al. 2015b). A companion project using the Wise 0.7-m Jay Baum Rich Telescope of Tel Aviv University addresses the deep imaging of edge-on disk galaxies and Hickson compact groups and is underway (P.I. N. Brosch).

The present image quality is 2.5 – 3” and poses no impediment to imaging low surface brightness features typically > 60” in size. Remote operations are now routine for the Jeanne Rich C28 telescope. Most of the dataset we report on here was obtained using an SBIG STL 11000 CCD which includes a guide CCD alongside the main detector. This

camera also has an internal filter wheel that holds 5 round 50mm filters. The detector is thermoelectrically cooled to typically –25°C; the detector is a KAI1100M interline transfer CCD with 9 μm pixels in a 4008 × 2672 pixel format. The scale is 0.83 arcsec/pix with a field of view of 0.57 sq. degree. The STL11000m camera has a readout noise of 13e[−], and the A/D conversion (single binned) is 0.8e[−]/ADU, and double-binned (a minority of our images) is 1.6e[−]/ADU. The FLI09000 used for a subset of our data has 11e[−] read noise in the 1MHz readout mode and close to 1.0e[−]/ADU. About 20% of our data are double-binned and so indicated. The compact design of this camera with the internal filter wheel results in images with only modest vignetting near the corners. The noise in these images is dominated by the sky background, usually ~ 2000 counts, on a given frame.

Since early 2015, we have used an FLI09000 detector on loan from Arizona State University; it is nearly identical to the STL11000m, with a 3056 × 3056 pixel format, lower read noise and 12μm pix. Guiding for the FLI camera is accomplished via a Lodestar X2 guide CCD mounted on an Astrodon Mega MOAG off-axis guider, in front of the filter wheel. We use a Finger Lakes Instruments CFW2 five position filter wheel that holds 2 inch square filters (currently supplied by Astrodon). In order to address some low level image persistence issues, data taken after mid-2016 employs the slow (1 MHz) readout mode using an RBI (Residual Background Image) flood with 400 ms flood time, 4 flushes, and a bin factor of 4, accessed via “advanced camera settings”.

Although persistence is an issue with the FLI camera, it can be eliminated by using the RBI Flood read mode, which preflashes the imager at the expense of a slight increase in read noise; in any case nearly all of the data we report here were obtained using the SBIG camera. The FLI Camera operates behind the off-axis guider and filter wheel; this results in greater vignetting than experienced for the STL11000m, however, we are able to flat field our images successfully and our exposure times overcome the modest loss of light due to vignetting. Our telescope operation and acquisition software is The Sky 6 by Software Bisque and is used for telescope control, Maxim DL version 6 for CCD camera control, and the commercial software Focusmax controlling a robofocus unit, for focus control. Temperature, humidity, sky darkness, and clarity are monitored using a Boltwood cloud sensor from Cyanogen, Ltd.

2.2 Observations and Data Reduction

The imaging reported in this paper uses a luminance filter, a square bandpass filter from 4000 – 7000 Å with an actual transmission equivalent very approximately to the full SDSS (Sloan Digital Sky Survey, Ahn, et al. 2014) *g* and *r* passbands. Its speed enables us to exploit good conditions and to build a large data set rapidly. We calibrate this filter using photometry of stars from the SDSS in the field of our target galaxies; this is described in Rich et al. (2012). We have concluded that the time needed for two-colour integrations is worthwhile only in exceptional cases; the errors in *g* – *r* become significant at 25–26 mag/arcsec² (Van Dokkum et al. 2014; Merritt et al. 2016). Our objective is to build a large sample of systems with well-measured stellar envelope luminosities, diameters, morphologies, and satellite properties.

³ www.astro-electronic.de/fs2.htm

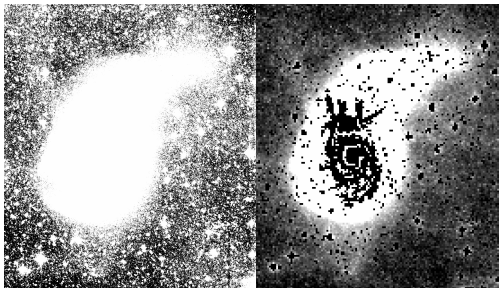


Figure 1. A comparison between our Luminance image of M51 using the C28 and SBIG11000m imager for 12×300 sec (left) and V band exposure courtesy of A. Watkins (Watkins et al. 2015) 31×1200 sec (roughly 10 hours) using the 24/36-inch Burrell Schmidt at Kitt Peak (right). Two completely independent approaches to deep imaging are reaching similar depths and revealing similar low surface brightness morphology. This result also addresses concerns that wide angle, faint scattered light might affect our measurements. Both figures show a limiting surface brightness of ~ 30 mag/arcsec². The dark inserted feature shows the approximate extent of the higher surface brightness portions of M51. The Burrell Schmidt image has had bright stars subtracted while ours has not.

A single passband enables these science goals and facilitates follow-up multi-wavelength studies if such follow-up appears to be compelling.

We obtain typically 12 – 36 images of 300s duration for each target. For the case of NGC 128, we measured its diameter for a coadd of 3 and 9 exposures respectively. We found that the 3 exposure coadd resulted in a 0.1 arcmin smaller diameter than the 9 exposure coadd, which is less than a 3% change, which is smaller than our other sources of error. These are randomly dithered during acquisition by ~ 20 arcsec on each move. We attempt to image galaxies near the meridian and avoid results with image quality poorer than 4 arcsec. The MaximDL acquisition software (<http://diffractionlimited.com/product/maxim-dl/>) includes a guiding control package, and this is employed using the Starlight express off-axis guider. As the CCD camera is cooled thermo-electrically only to a temperature ranging from -20 to -40°C , there is still dark current, and we must also acquire dark frames of equal length to the images, at the same temperature as the image frames. These calibrations, along with bias and flat fields, are acquired every few nights. We obtain flat fields frequently, usually every few nights, using the 76 cm square Alnitak XL electroluminescent panel, finding no difference between using the panel and twilight flats. We use an SBIG 340C all sky camera to monitor climate and transparency, and we do not take data in moon or even light cirrus. We verify that the sky is essentially photometric before and during imaging and observations during any moonlight is avoided.

All data are reduced using standard IRAF routines including the subtraction of 300s darks obtained at the same operating temperature as the science frames. In the rare cases where the flat fielding is not optimal, we use the IRAF routine IMSURFIT to arrive at a final flattened background. IMSURFIT fits two-dimensional low order polynomials to

the sky background; we limit the polynomial to order < 5 and confirm that the application of IMSURFIT does not affect our derived surface brightness profile or measurement of envelope diameter. It was also very rarely necessary to add a small constant to the frame to avoid oversubtraction. We conclude that our agreement with other studies as evidenced by Figs. 1-5 reassures that our instrumentation and reduction procedures reach the standards of other similar studies.

2.3 Surface Photometry

The image preparation was done employing a procedure developed by one of the authors (A. Mosenkov) as follows.

An initial step was including astrometry using the website Astrometry.net⁴.

Then we performed photometric calibration using a range of photometric sources. In each frame, isolated, non-saturated stars with a high signal-to-noise ratio were automatically selected (an average number of such stars for all fields was 59). Then we cross-correlated the selected stars with photometric databases of SDSS, Pan-STARRS (Chambers, et al. 2016; Flewelling, et al. 2016), and *Gaia* DR2 (Gaia Collaboration, et al. 2016, 2018) and transformed their measured magnitudes to the SDSS *r* band using Finkbeiner et al. (2016) and sec. 5.3.7 from the *Gaia* data release documentation⁵ and taking into account Galactic extinction using a 3D dust map from Green, Schlafly, Zucker, Speagle & Finkbeiner (2019)⁶. The average calibration error is 0.046 mag. Third, sky was carefully estimated for a sub-field, which includes the target galaxy and some empty background (typically, we used a box with a side 5 times larger than the galaxy diameter). We used SEXTRACTOR (Bertin & Arnouts 1996) to create a segmentation map for this sub-field and mask out all detected objects. To minimise the impact of the scattered light from the masked objects on the sky fitting, the SEXTRACTOR mask for each object was increased by a factor of 1.5. We then used this mask to fit the sky with a polynomial of some degree, starting from 0 (constant sky level) to 5 (significantly non-linear sky background), increasing this value after each iteration if the sky-subtracted image still had a gradient. Additionally, after subtracting the best-fit polynomial from the original image, we re-estimated the sky within an elliptical annulus, built around the galaxy on the basis of the preliminary 1D azimuthally-averaged profile where the profile flattens (typically, at a radius of the double optical radius R_{25} with an annulus width of 32 pixels). Also, to estimate background variations within the annulus, which can be left after flat-fielding or caused by scattered light from stars, extended objects (satellite galaxies), Galactic cirrus, or low surface brightness features (tidal streams, stellar flows etc.) we determined the variations of the median (using 3σ clipping) inside uniformly located boxes with a side of 32 pixels placed along the annulus. We define the standard deviation of the measured median values within these boxes as the background estimation error. Note that it is different from the

⁴ <http://nova.astrometry.net/>

⁵ <https://gea.esac.esa.int/archive/documentation/GDR2/>

⁶ <http://argonaut.skymaps.info/>

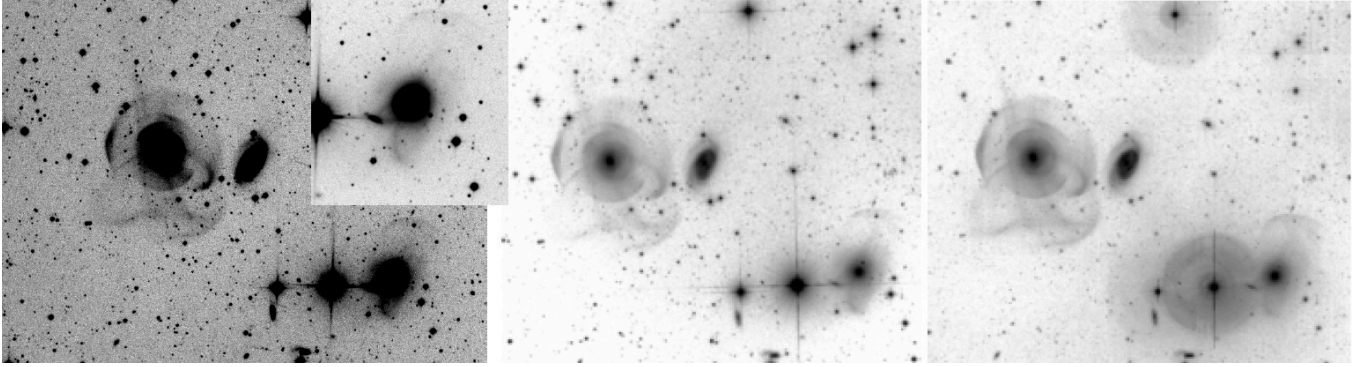


Figure 2. Images of NGC 474 and 470 using different platforms, each showing the faintest features at ~ 29 mag/arcsec². This illustrates our excellent scattered light control; see also the inset of arcs associated with a galaxy interacting with the elliptical galaxy NGC 467 (Left): 25×300 sec exposure (SDSS g) using the Jeanne Rich 28-inch telescope. (Middle) A 21.5 hour exposure using the Irida Observatory 12-inch astrograph; (Right) 0.7 hour exposure in SDSS g using the Canada-France-Hawaii Telescope (middle and right-hand panels from [Duc et al. 2015](#), fig. 7). Notice the scattered light in the 3 bright images at lower right, and our clean detection of the faint arc.

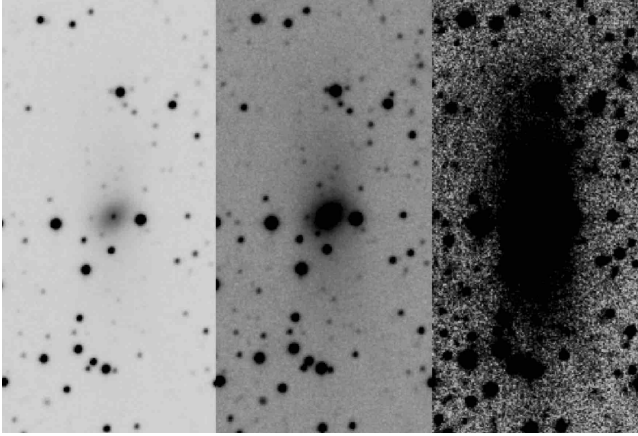


Figure 3. The nucleated dwarf galaxy associated with NGC 7331 at RA 2000: 22h 37m 12.4s, DEC 2000: $+34^\circ 37' 12.1''$. The tidal tails were first reported in [Paudel & Ree \(2014\)](#) where the galaxy is HdE6. N is up and E to the left. The full frame height is 6 arcmin; the suspected tidal tail feature appears as nearly vertical wings. In this 12×300 s exposure, the dwarf is illustrated at 3 different stretches (compare with fig. 2 of [Blauensteiner et al. 2017](#) from a 26 hour exposure). The full extent of the dwarf is $1 \times 4'$, corresponding to 4×16 kpc at the 14 Mpc distance of NGC 7331. [Duc, Cuillandre, Renaud \(2018\)](#) (their figs 2 and 3) also illustrate this galaxy and show the same extended tails, but do not explicitly mention the galaxy or this structure.

standard deviation of the sky level, which is measured for the background within the whole elliptical annulus.

Finally, galaxy images were cropped to encompass the outermost galaxy isophotes plus some space beyond them (1.5 times larger than the diameter of the outermost isophotes).

To generate surface brightness profiles for a galaxy, we used the following technique. We masked out all foreground stars and other galaxies detected in the final frame. For this, we used the masks, which had been produced earlier, and revisited them by eye. Also, to them we added masks created

for the space inside the galaxy by searching for local maxima above the 2D galaxy intensity profile.

For each frame we estimated the Point Spread Function (PSF) for those stars which we used for photometric calibration. Then we performed GALFIT ([Peng, Ho, Impey & Rix 2002, 2010](#)) fitting of each galaxy image using a single Sérsic model ([Sérsic 1968](#)), convolved with the corresponding PSF. From this modelling, we were able to estimate general parameters of the galaxy position and orientation (position angle) and its ellipticity. We used these values as an initial guess for the IRAF/ELLIPSE routine. We performed isophote fitting starting from the center and extending up to the outermost isophote which can be detected in the galaxy. The galaxy center, position angle and ellipticity in each fit were set free. From the output results of the ellipse fitting we created azimuthally averaged profiles which were corrected for Galactic extinction using [Schlafly & Finkbeiner \(2011\)](#). The profiles will be presented in detail and discussed in a future work, while here we only use them to estimate the galaxy diameter (see Sec. 3.3).

2.4 Scattered light issues and reproducibility of HERON

Amateur operated telescopes of professional quality contribute data that reach $29\text{--}30$ mag/arcsec² in tens of hours of integration ([Javanmardi et al. 2016](#)); the 8 lens Dragonfly array attained 32 mag/arcsec² in 35 hours and it is reasonable to assume that a 24 lens array reaches these levels in half the time. Our single detector at the f/3.2 prime focus with a 0.7-m primary is able to detect all of the faint companions reported by [Javanmardi et al. \(2016\)](#), all except the faintest details in M 101 reported in [Van Dokkum et al. \(2014\)](#), and all faint extensions detected in 10 hr by the 24/36-inch Burrell Schmidt in M 51 ([Watkins et al. 2015](#); Fig. 1). We also detect all of the streams reported in [Miskolczi et al. \(2011\)](#). At the faint levels we work ($29\text{--}30$ mag/arcsec²) it is reasonable to be concerned that wide-angle scattered light might compromise our ability to image and measure faint structures. We have compared our deep images and surface brightness profiles with other work (e.g. [Watkins et al.](#)

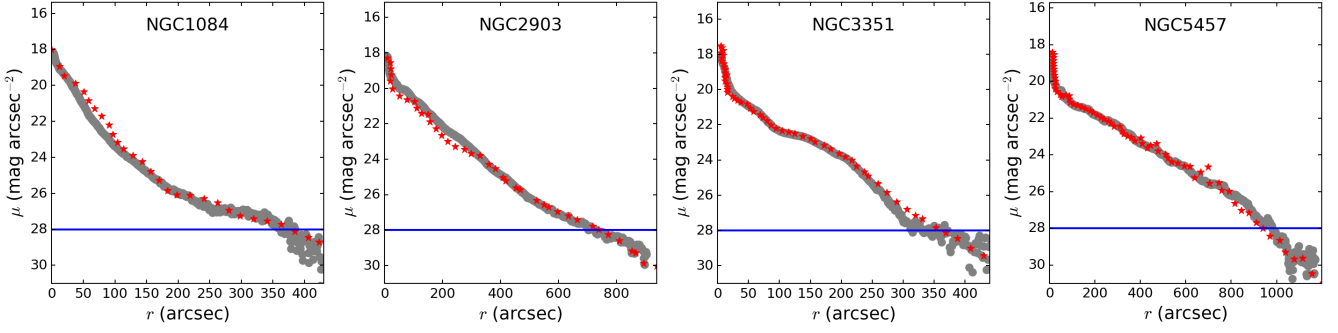


Figure 4. Comparison of our measured surface brightness profiles (grey) for four common galaxies with those observed by Merritt et al. (2016) (extracted from their paper using <https://apps.automeris.io>). There is excellent agreement between the surface photometry of HERON and those of Merritt et al. (2016). Our data reach to $\mu \sim 29 - 30$ mag/arcsec². The blue line shows the 28 mag/arcsec² isophote, at which we measure the envelope diameter.

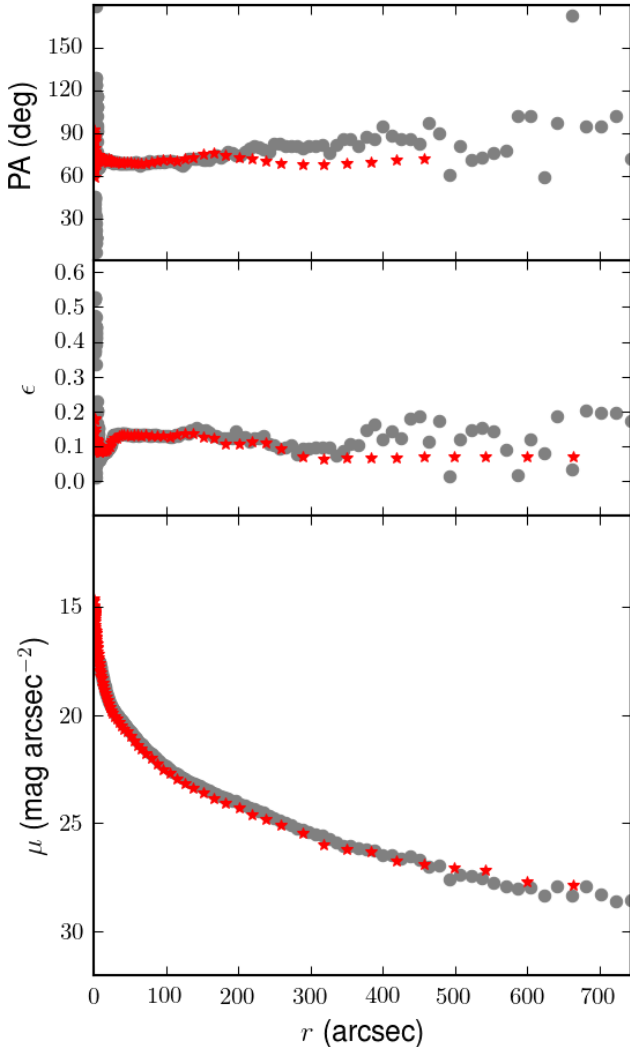


Figure 5. Comparison of our surface brightness profile of NGC 3379 with that of Kormendy et al. (2009) (red stars). HERON are data illustrated in grey. Our data reach to $\mu \sim 28.5$ mag/arcsec².

2015; Fig. 1) and Merritt et al. (2016). These two programs are respectively from the Burrell Schmidt and Dragonfly array, and they report surface photometry to 30 mag/arcsec². We also note the excellent agreement between low surface brightness details for NGC 4449 and its tidally-disrupting dwarf galaxy companion NGC 4449B illustrated in Rich et al. (2012) and Martínez-Delgado et al. (2012). Fig. 2 compares our 12 × 300s exposure of NGC 474 with a 21 hour exposure from the 30-cm astrograph of Irida Observatory⁷ and the CFHT (Canada-France-Hawaii Telescope; 0.7 hours g-band exposure; both of these illustrated in fig. 7 of Duc et al. 2015). An example of the performance attained by our system, reaching ~ 29 mag/arcsec², is shown by the tidal structures revealed in Müller, et al. (2019).

Duc et al. (2015) emphasized that the CFHT has serious scattered light halos not present in the long exposure using the astrograph at Irida Observatory. Our 0.7-m C28 telescope shows exceptionally low scattered light, as good as that of the astrograph and substantially better than the raw CFHT image. The comparison illustrated in our Fig. 2 with that of fig. 11 in Duc et al. (2015) shows that our images can reach at least 29 mag/arcsec² in surface brightness. While not illustrated, our HERON imaging of Stephens Quintet reproduces all of the faint structure detected by Duc, Cuilandre, Renaud (2018) also using the CFHT telescope. Significantly, however, Fig. 2 convinces us that our control for scattered light is excellent, reaching or exceeding that of the Irida Observatory astrograph (Duc et al. 2015). Additional comparisons with ~ 10 hour long images obtained using an 8-inch doublet refractor confirm our excellent scattered light control (B. Megdal, private communication). Example images and comparisons are available on the HERON website at IRSA. We will not further discuss the scattered light issue in this paper as it has no impact on our measurements or conclusions.

Fig. 3 illustrates our image of a dwarf galaxy near NGC 7331. Blauensteiner et al. (2017) published images ranging from 6 to 21 hours in depth, however, the tidal tail was actually discovered from SDSS3 images by Paudel & Ree (2014). Here, we are able to discern the full extent of the tidal structure (right panel) reaching 4 arcmin = 16 kpc in total length, making it one of the largest known tidally

⁷ www.irida-observatory.org/

Table 1. Envelope diameter comparisons between the *HERON* measurements (at the level of 28 mag/arcsec²) and those from Merritt et al. (2016). We only compared galaxies that were in both samples, except for NGC 4258 (see text). The radii were measured on the basis of Fig. 4.

NGC	<i>HERON</i> Diameter kpc	Merritt et al. Diameter kpc
1084	27.2	28.0
2903	32.6	33.5
3351	16.9	17.4
M101	33.8	32.5

affected galaxies; our measured size is over a factor of 2 larger than that of Paudel & Ree (2014). We also recover the large tidal tails that can be noted in the CFHT images of Duc, Cuillandre, Renaud (2018) (their figs. 2 and 3), but those authors did not explicitly note the object. This tidal feature is twice the extent of NGC 4449B, the tidal dwarf near NGC 4449 (Rich et al. 2012). *We have confidence in our data quality because our low surface brightness features are detected by other investigators using different telescopes and reduction methods. We have not failed to measure any features reported by others in the literature.*

In Fig. 4 we illustrate the exceptionally good comparison of our surface brightness profiles with those of 4 galaxies in Merritt et al. (2016). One galaxy, NGC 4258, is excluded from the comparison as our image does not cover its outskirts, and, hence, our profile is cropped. Table 1 presents our agreement in diameter measurement with Merritt et al. (2016). Fig. 5 compares our surface brightness profile of NGC 3379 with Kormendy et al. (2009) and we attain very good agreement to 28 mag/arcsec². Note that in Figs. 4 and 5 the original profiles from Merritt et al. (2016) and Kormendy et al. (2009) were shifted upwards to match the inner part of our profiles (excluding the very center where our observations can be saturated), as their observations were done in the *g* and *V* band, respectively.

In Sec. 3.3.1 we consider the impact of the extended PSF on the measured diameters.

3 ANALYSIS

3.1 Sample

Most of our galaxies were selected from the Two Micron All Sky Survey (2MASS) Large Galaxy Atlas (Jarrett et al. 2003). We also observed a smaller sample of nearby low luminosity galaxies selected to have large angular diameters from the Karachentsev et al. (2017) catalog, and with more distant early type galaxies from the ATLAS3D survey.

While *HERON* is by no means intended to be a volume-complete survey, we note that our sample encompasses ~1% of the galaxies in the Local Volume within 50 Mpc, given in White et al. (2011).

Fig. 6 shows the distribution of absolute magnitudes of our final sample, sorted by Hubble type. Although our sample has a large number of relatively nearby galaxies, it is dominated by galaxies with $M_V < -20$. We are addressing that shortcoming by observing low luminosity galaxies selected from the Karachentsev et al. (2017) catalog.

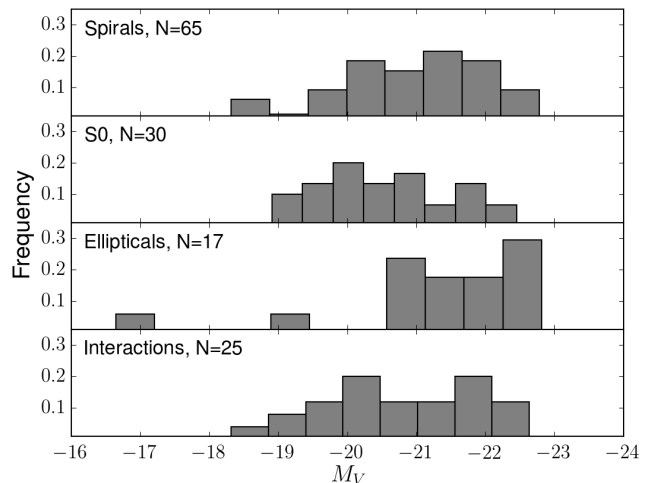


Figure 6. The *V*-band absolute magnitude (M_V) distribution for the *HERON* sample, divided by Hubble type. The sample labelled as “interactions” represent the subset of our sample displaying interaction signatures.

3.2 Depth of the images

Based on the created averaged surface brightness profiles (see Sec. 2.3), we determined a limiting surface brightness level for each sample galaxy where the error of the intensity is comparable to its value. These values are listed in Table B2.

Fig. 7 shows a histogram of the limiting surface brightness levels. The distribution looks normal with a mean surface brightness of $\sim 28.8 \pm 0.5$ mag/arcsec². 115 galaxies (97%) have limiting diameters at surface brightness levels deeper than 28 mag/arcsec² and 37 (31%) deeper than 29 mag/arcsec². It appeared that four galaxy images in our sample (NGC 525, NGC 4258, NGC 7465, and UGC 4872) do not demonstrate deep profiles (their limiting surface brightness is higher than 28 mag/arcsec²). Therefore, we do not consider them in our further analysis.

As the vast majority of our sample galaxies have surface brightness profiles that extend to 28 mag/arcsec² and deeper, we decided to define the diameter of the envelope/halo at this level. Further, we will refer to it as the envelope diameter. Alternatively, we will use the envelope radius as half the envelope diameter.

3.3 Diameter measurements and magnitudes

We find that one of the most reliable and reproducible features is the measurement of the diameter as determined at a fixed surface brightness level. As defined above (see Sec. 3.2), the envelope diameter (radius) is measured at the 28 mag/arcsec² isophote, as almost all galaxies in our sample have surface brightness deepness up to this isophote. As some systematic errors may potentially influence the measured diameter, such as the uncertainty of the background measurement, the calibration error, the local error of the IRAF/ELLIPSE model, we used Monte Carlo simulations to model galaxy profiles with taking into account all these errors. This allowed us to estimate an error on the diameter.

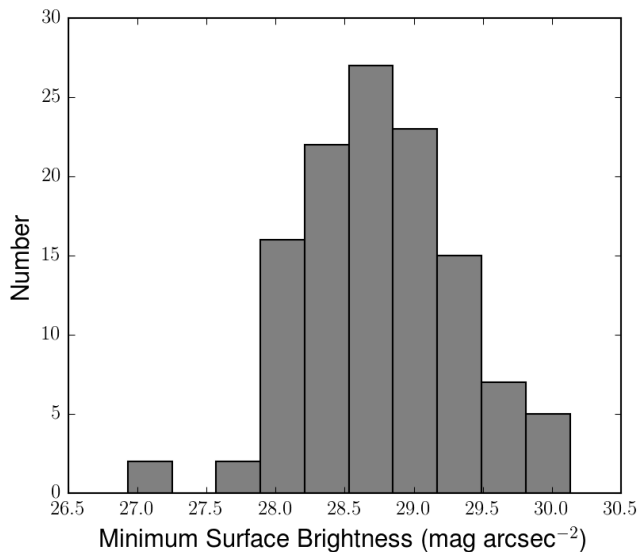


Figure 7. Histogram displaying the corresponding surface brightness that our diameter measurements reached. The histogram displays a mean value of $28.8 \text{ mag/arcsec}^2$ and a standard deviation of 0.5 mag/arcsec^2 .

We calculated that an average error of the envelope diameter for the whole sample is $3.4 \pm 1.6 \%$ of the diameter value. In Table B3 we provide the diameter values and its errors, along with the envelope shape which was visually estimated for each galaxy. We are about to discuss these envelope shapes in our subsequent study.

An example of a diameter measurement at two surface brightness levels, 28 mag/arcsec^2 and $29.4 \text{ mag/arcsec}^2$ (the limiting surface brightness level for this galaxy), are illustrated in Fig. 8 and Fig. 9.

In order to report a physical diameter and absolute magnitude, we must adopt a distance. In this work, we use the redshift-independent distances provided by the HyperLEDA database⁸ (Makarov et al. 2014). For galaxies without redshift-independent HyperLEDA distances, we use the redshift-independent distances provided by the Nasa/ipac Extragalactic Database (NED)⁹ or the flow-corrected redshift-derived values provided by NED (if no redshift-independent distances are provided).

As some of our galaxies may have saturated nuclear regions, we do not use our photometry to measure galaxy fluxes. Instead, we adopt from HyperLeda the magnitudes m_V and the colours $B - V$, denoted as btc and $bvtc$. These have been corrected for Galactic extinction using Schlafly & Finkbeiner (2011) and internal absorption (see comments in HyperLeda).

3.3.1 Impact of the PSF on our measurements of the diameter

As the PSF can significantly affect the real galaxy profile (see e.g. Sandin 2014, 2015), we need to ensure that our

⁸ <http://leda.univ-lyon1.fr/>

⁹ <https://ned.ipac.caltech.edu/>

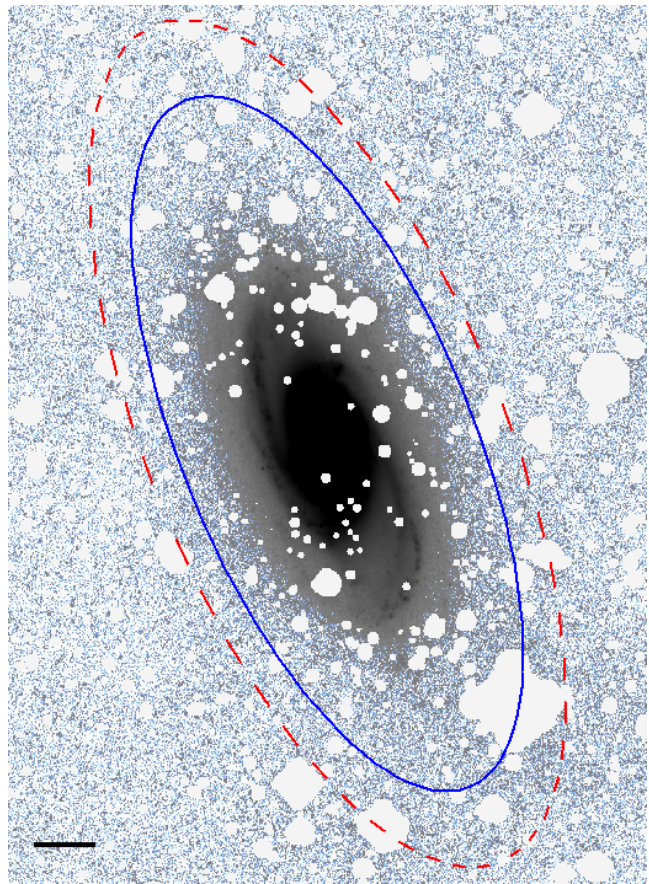


Figure 8. This figure displays two envelope diameters for the SABbc galaxy NGC 2903 (see also Merritt et al. 2016). The blue solid ellipse is related to the isophote 28 mag/arcsec^2 , whereas the red dashed ellipse is related to the $29.4 \text{ mag/arcsec}^2$. NGC 2903 has a diameter of $24.1 \pm 0.6 \text{ kpc}$ at $M_V = -21.57$. This figure is intended to display the lowest surface brightness we reached; other images with scale bars are shown in the Appendix A, Fig. A1. The scale bar in the left bottom corner shows $2''$.

measurements of the diameters do not suffer from this effect. For this purpose we should use an extended PSF, where extended wings should be larger than 1.5 times the distance between the outermost galaxy isophote (in our case it is 28 mag/arcsec^2) and the center, where we usually observe the maximum intensity. To take into account the PSF effect, two approaches are used. The first method includes a multi-component modelling of the galaxy using the convolution with an extended PSF (Trujillo & Fliri 2016). The second approach uses deconvolution techniques (see e.g. Karabal et al. 2017). As our sample consists of a rather large number of objects of different orientation, morphology and angular size, the first approach is extremely time consuming. The second approach is more promising, taking into account a constantly increasing computational power to solve such kind of problems. This work has to be done in the future.

In this study we decided to investigate the effect of an extended PSF on our galaxy profiles by performing simulations of galaxy images and then convolving them with the extended PSF.

To create an extended PSF for the HERON, we used

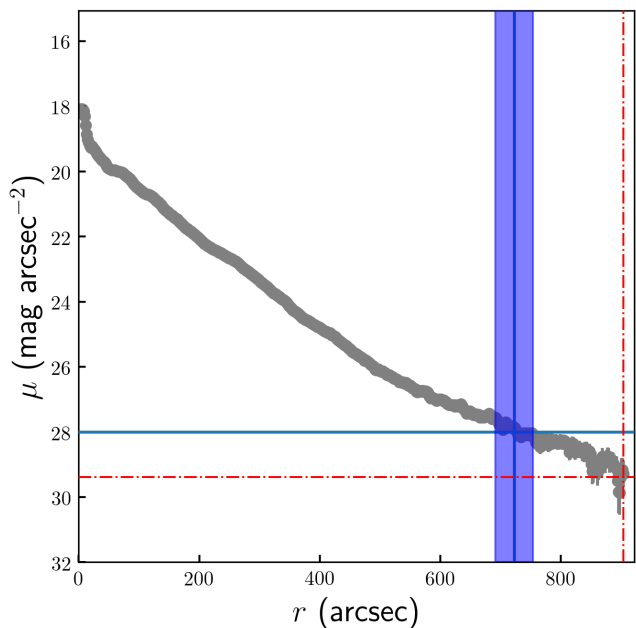


Figure 9. Example of the envelope radius measurement for NGC 2903. The blue solid horizontal line shows the surface brightness level 28 mag/arcsec^2 , whereas the red dot-dashed horizontal line shows the limiting surface brightness level for this galaxy ($29.4 \text{ mag/arcsec}^2$). The vertical lines show a measure of the envelope radii at these levels. The blue stripe for the radius of the 28 mag/arcsec^2 isophote includes different systematic errors (see text).

an observation of the bright star HD 9562. Using the IRAF/ELLIPSE routine, we created its azimuthally averaged profile up to a radius of $\approx 1000''$. However, as its central part is saturated, we replaced the core of the extracted profile by a non-saturated star (the normalization was done at the intersection of the profiles, see Karabal et al. 2017 for details). The synthesized profile is shown in Fig. 10.

As in our sample there is a large variety of morphologies, let us consider three simple models of galaxies: with the Sérsic index $n = 1$ (late-type galaxy), 2 (galaxy with a compact bulge) and 4 (elliptical galaxy). Other parameters of the Sérsic model are: the effective radius is $47''$ and the effective surface brightness is $21.2 \text{ mag/arcsec}^2$ (these are the average values for our sample determined from our GALFIT decomposition, see Sec. 2.3). The 2D images were simulated with GALFIT and then convolved with the extended HERON PSF. The results of the envelope radius estimation are shown in Fig. 11. As one can see, the overestimation of the real radius at the 28 mag/arcsec^2 isophote is very small (less than 1.5% for all n). However, it is getting larger for lower surface brightnesses: for the 30 mag/arcsec^2 isophote an overestimation increases up to 5.5% for $n = 1$. From this comparison it is obvious, that our measurements of the envelope radius are within the typical errors of the envelope radius, and cannot affect our results. We should notice, however, that the presence of an AGN may change this conclusion as the bright compact source will produce extended wings which can be mis-interpreted as a halo. However, only 12 galaxies in our

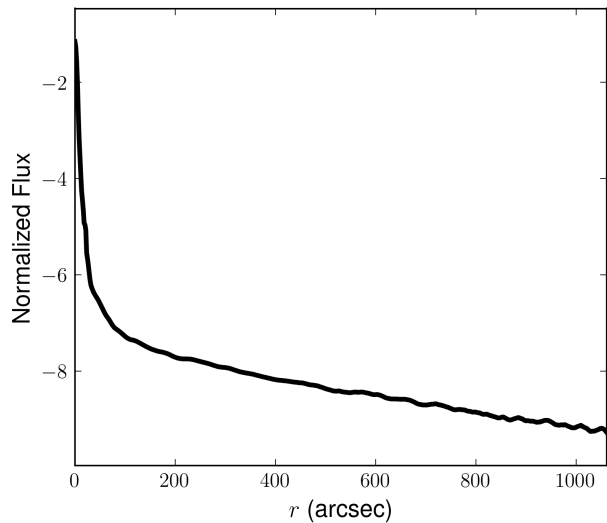


Figure 10. Normalized azimuthally-averaged profile of the PSF model profile.

sample exhibit some activity at the center, therefore, we do not consider this case.

3.3.2 Tests of our diameter measurement metric

In order to reassure us that our measurement of diameters is robust and does not arise due to a selection effect, we have performed a number of tests on the data.

Fig. 12 shows that there is no correlation between diameter and apparent V magnitude. If scattered light from bright central bulges or disks were a significant contributor to our measurement of diameter, one might expect to see a correlation between diameter and apparent magnitude. Fig. 13 presents our correlation between diameter and radial velocity. Again, no strong correlation is expected. However, our most distant galaxies include some of our most luminous. Fig. 14 considers absolute magnitude vs. radial velocity. Our sample is under represented at the faint end; as mentioned previously we are taking steps to address this. We conclude from these tests that our measurements of diameter do not suffer from any systematic trends, and they do not behave as expected if the diameter measurements were seriously affected by scattered light or systematic error.

4 DISCUSSION

We now address how our measurement of envelope diameter correlates with various physical properties of galaxies in our sample. We first consider the characteristics of our sample as a whole in Fig. 15. S0 and spiral galaxies span the widest range in luminosity. Although our most luminous galaxies are elliptical, the absolute magnitude distribution of galaxies by Hubble type and presence of interaction signatures is remarkably similar.

Fig. 15 shows a strong primary correlation between the measured physical diameter of the envelope, and absolute V magnitude, agreeing with our work earlier reported in Rich et al. (2017). We have confirmed this trend based on diameters at 25 mag/arcsec^2 (D25) from the NED Database. The

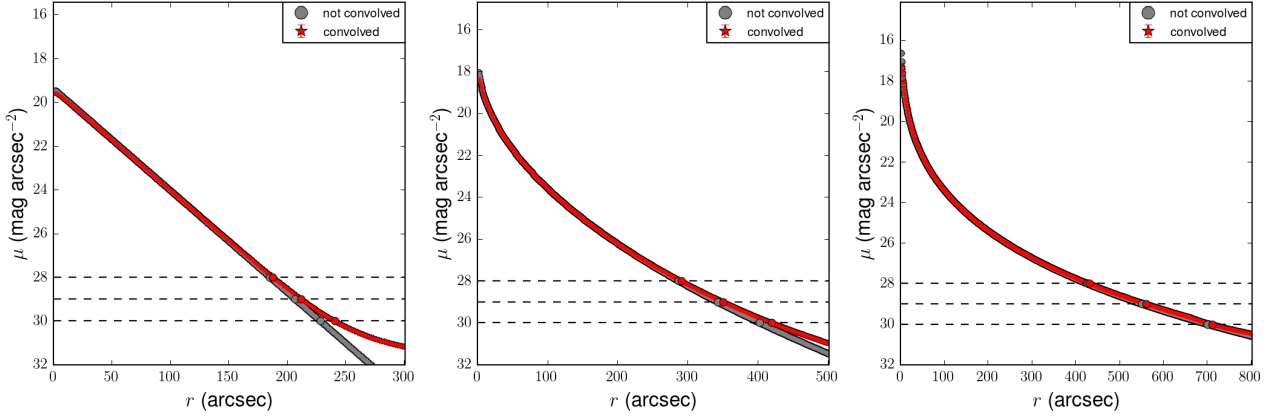


Figure 11. The comparison of the original (non-convolved) and convolved profiles for three Sérsic models with $n = 1$ (left), $n = 2$ (middle) and $n = 4$ (left). The dashed lines show some characteristic surface brightness levels of 28, 29 and 30 mag/arcsec².

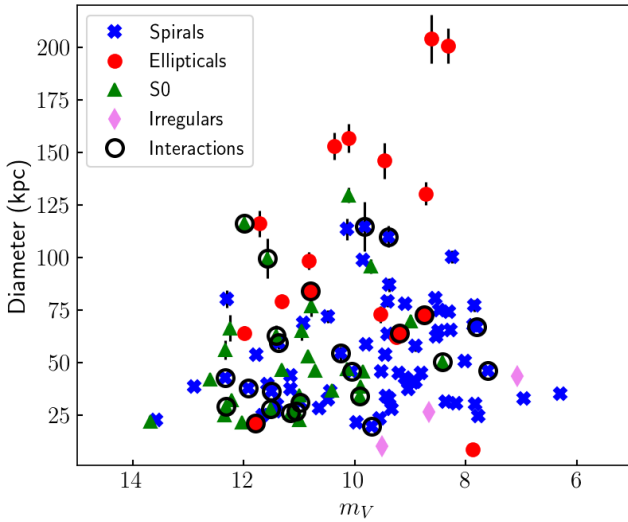


Figure 12. Envelope diameter (kpc) versus apparent V magnitude. We do not see any trend, as expected if scattered light does not contribute to the measured envelope diameter. The apparently brightest galaxies might in principle have spuriously larger diameters caused by scattered light from their e.g. bulge or disk components.

D25 data confirm the general trend but as expected, do not reach the largest diameters. Similarly, our work confirms the work of [Muñoz-Mateos et al. \(2015\)](#) that finds similar trends in galaxy diameter and stellar mass from Spitzer data. Our data show an apparent transition near $M_V \sim -20.5$ or L^* at which point a subset of galaxies, mostly E and S0, begin to display very large diameters, reaching 150 kpc. However, a few spirals also have large envelopes, as previously noted by [Kormendy & Bahcall \(1974\)](#). We find no tendency for interactions to be detected in a particular magnitude range, except for their relative paucity for $M_V > -20.5$. This trend is not a simple correlation between galaxy diameter and total mass. For example, at $-20 < M_V < -24$, galaxies of all morphological types exhibit a total range in measured diameter from 20 to 170 kpc and within this most luminous category there is only weak dependence of diameter on luminosity.

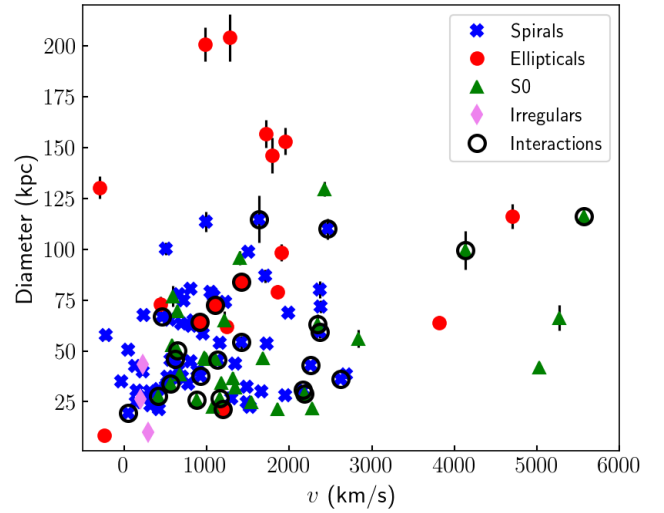


Figure 13. Envelope diameter (kpc) versus radial velocity with galaxy classification indicated. No trend is evident; the distant galaxies with large halos correspond to luminous systems that are more rare in our lower redshift sample. The lack of any strong correlation of halo diameter with velocity is expected.

When plotted as log Diameter vs. stellar mass in Fig. 16, the apparent break at L^* is not as evident; we also observe a trend similar to that found by [Muñoz-Mateos et al. \(2015\)](#). This plot also suggests that ~ 200 kpc may represent an upper limit to envelope diameter, although more observations are required to confirm this. One very large envelope with diameter ~ 170 kpc has been found surrounding Hickson group HCG 98 and is reported in [Brosch et al. \(2019\)](#). It will be important to explore whether these correlations extend to the total luminosities encompassed in small galaxy groups.

4.1 The Galaxy Colour–magnitude diagram

We turn next to explore correlations across the galaxy colour–magnitude diagram. Our motivation is to explore whether the signatures of active interactions preferentially populate any part of the CMD. Fig. 17 shows that galaxies

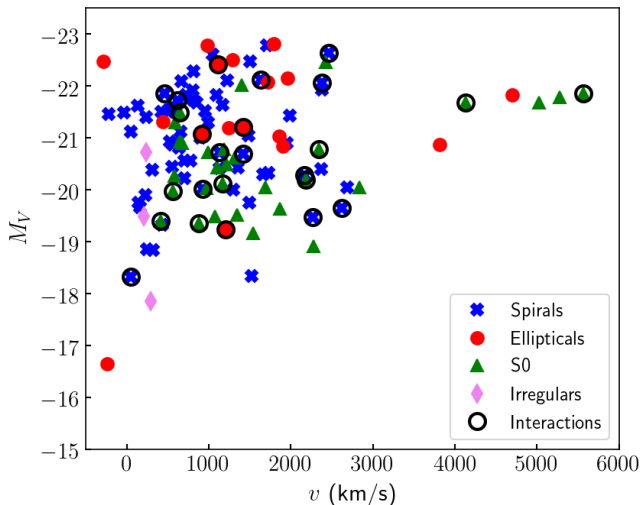


Figure 14. A plot of absolute V magnitude (M_V) versus radial velocity. The sampling in absolute magnitude and radial velocity shows no apparent bias. The present sample is relatively sparse at the low luminosity end; this will be supplemented using the Karachentsev et al. (2017) catalogue, as described in the text.

hosting interaction signatures (Duc 2017) appear to show no preference for populating the blue or red sequence, or the green valley. Interactions may be a significant factor in driving quenching, as the significant infall of baryons and dark matter might be expected to be a factor that induces star formation.

Fig. 18 shows a new result: the largest envelopes appear to preferentially populate the luminous end of the red sequence and include both S0 and E galaxies. However, large halos are also seen in the blue cloud. We previously found that the envelope size is correlated with luminosity and recall that Fig. 20 shows that elliptical galaxies host the largest halos; hence the largest envelopes are found in $M_V < -21$ galaxies on the red sequence.

However, the largest envelopes are not *confined* to the red sequence, with the most luminous blue sequence members and at least one green valley galaxy exhibiting large envelopes as well. It will be interesting to consider the role of environment in future work, however, it is noteworthy that only the bright end of the red sequence hosts the largest envelopes. There appears to be no clear preference for larger envelopes on the faint end of the red sequence compared to the blue cloud. The strong primary correlation between intrinsic luminosity and envelope size is of greatest importance, but for galaxies with $M_V < -21$, the envelopes of greatest diameter are found at the bright end of the red sequence and are notably less common in the blue cloud and green valley. Simulations also predict, at fixed stellar mass, more massive stellar halos in red galaxies than in blue (Elias et al. 2018). However, as noted originally by Kormendy & Bahcall (1974), the largest envelopes can be found in both spirals and ellipticals.

The cases of very large envelopes not on the red sequence are unusual. NGC 474 is an elliptical galaxy in the green valley, but it is involved with a significant (likely recent disk) merger event. The merger shells are bluish on

false colour images (see e.g. Duc et al. 2015); this galaxy will likely migrate to the red sequence after the merger event settles. NGC 5746 shows one of the largest envelopes found for a galaxy in the blue cloud. This edge-on, boxy/peanut shaped bulge galaxy has an extraordinary 60.3 kpc diameter envelope, and its rotation curve has the highest peak velocity in the Bureau & Freeman (1999) sample; ± 500 km/sec. NGC 772 is also identified as being in the blue cloud, but it is a face-on spiral with one spiral arm and 3 galaxies entrained in a stream; they all lie projected on a field of complex infrared cirrus. It is in the blue cloud by virtue of its disk, and hosts an extremely large envelope due to the ongoing interaction. NGC 474, NGC 772, and NGC 5746 are anomalous in their hosting of large envelopes yet not residing on the red sequence. The remaining largest envelopes clearly reside on the red sequence and are ellipticals and S0s.

In Fig. 19, we note that the largest envelopes are found in elliptical galaxies, but that galaxies with interactions host envelopes that span the full range of diameter. Larger samples will be required to assess whether interactions are found in specific circumstances e.g. small groups or close companions. Future work will also address low luminosity companions and their characteristics.

Fig. 20 shows the very clear difference in the distribution of envelope diameters when segregated by luminosity. It is clear that the bulk of galaxies with $M_V < -20.5$ have envelopes larger than those fainter, a statistic that is highly unlikely to change, even if the sample size were to increase. In Fig. 21 we present the histograms that correspond to an approximate red sequence/blue cloud colour cut in Fig. 18; this reinforces our claim that the largest halos are found on the red sequence.

5 THE NATURE OF ENVELOPES OF DISK GALAXIES

In Fig. 22, we ask whether projected orientation has an impact on the measured diameter of the envelope. We see that edge-on disks, and find no clear difference in projected sizes. We now turn to consider the possibility that the outermost detected light in face-on disks (e.g. Merritt et al. 2016) may arise from a disk population, and may not be a classical Population II halo.

The outer edges of spiral galaxies are broadly observed to divide between those showing evidence of star formation and spiral or flocculent spiral structure (e.g. M 101) and those showing a smooth outer extension (M 83). Fig. 23 illustrates these examples; they represent extremes, with star formation at the outer edges being the more common occurrence. M 51 presents a smooth but unusually shaped outer envelope, whereas M 74 and M 101 appear to show the more commonly seen spiral structure. In the case of M 83, the outer envelope is unusual in that it extends substantially beyond the disk, shows no spiral structure even in subtraction, and is oval and off-centred. This outermost structural feature suggests that (as is the case with M 51) its envelope is more likely to be a flattened disk-like projection.

Exploring further the question of which stellar population is represented in the outer parts of spirals, we present subtractions of the ELLIPSE models for galaxies that are discussed in Merritt et al. (2016). In Fig. 23, we can ob-

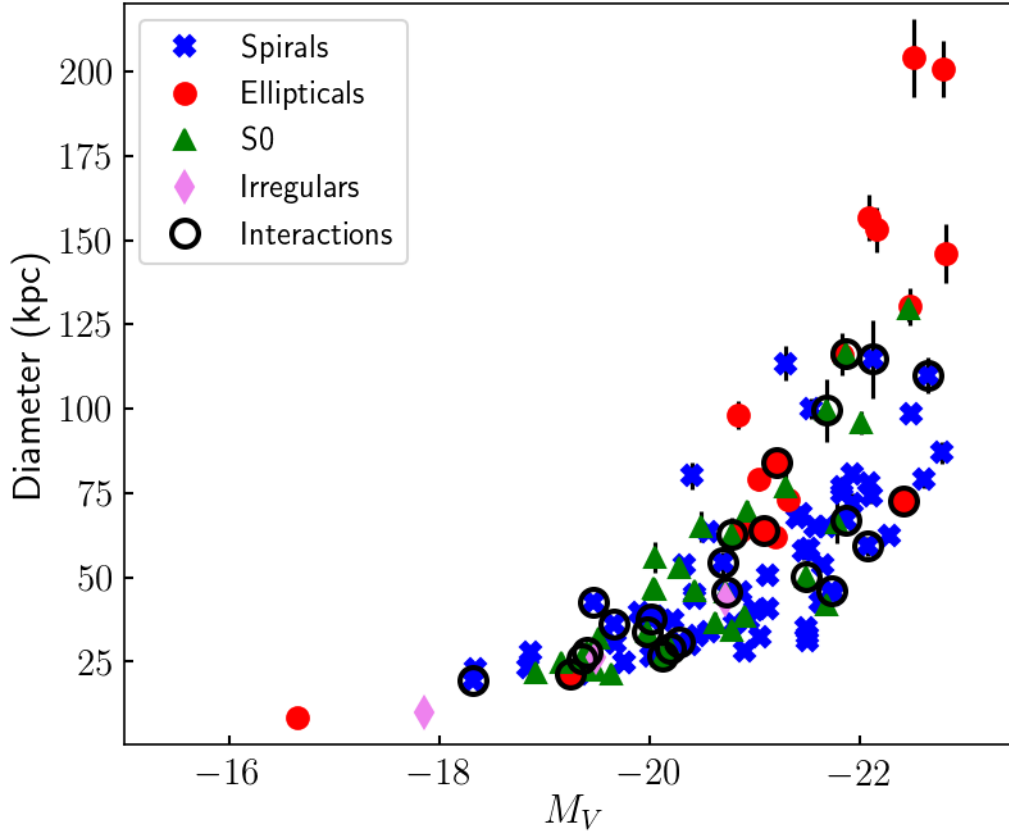


Figure 15. A plot of envelope diameter (kpc) versus absolute magnitude M_V . Galaxy classification is according to the symbols in the legend. Circled symbols indicate galaxies with a stream, extended shell, or otherwise strongly asymmetric interaction. The largest envelopes are found in the most luminous galaxies.

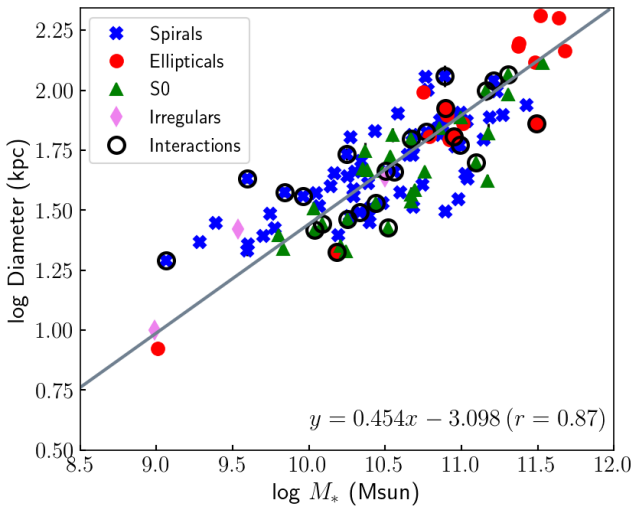


Figure 16. Log diameter in kpc vs stellar mass using the relationship of Bell et al. (2003). The trend extends to lower surface brightness that reported in Muñoz-Mateos et al. (2015)

serve that the outer regions of NGC 1084, NGC 3351, and NGC 2903 show clear spiral structure in subtraction. Using both imaging from the 0.7-m C28 telescope as well as verification images obtained by B. Megdal employing a single

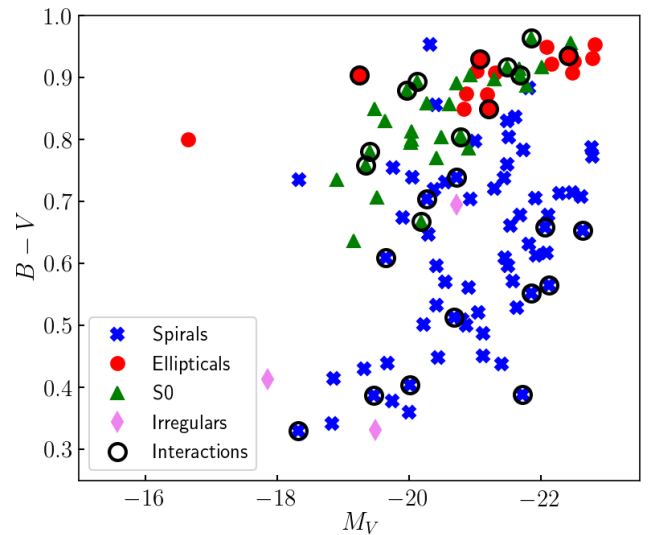


Figure 17. A plot of $B - V$ colour versus M_V . Circled symbols indicate interactions. The diagram divides cleanly into the luminous red sequence, green valley, and blue cloud. Interactions appear to occur throughout this plot and do not favour a particular location.

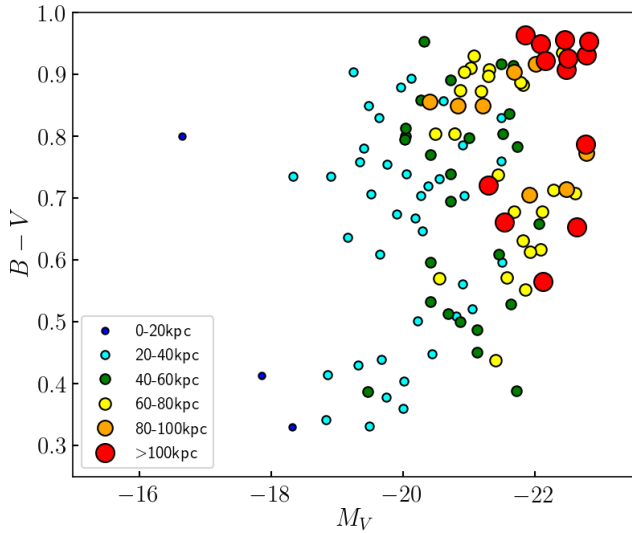


Figure 18. The same plot as Fig. 17, $B - V$ colour magnitude versus M_V . Here, the different coloured symbols represent different envelope diameters according to the legend. The bright end of the red sequence hosts the largest envelopes, those with diameter > 100 kpc, but the faint end of the red sequence has halo sizes comparable to that of the blue cloud. The largest envelopes are seen in the most luminous galaxies regardless of whether they occupy the blue cloud, green valley, or red sequence. Envelopes of median diameter can be found across the plot.

lens 8-inch refractor (to reduce scattered light issues), we do not detect envelope light outside of the extreme edge of the disturbed disk (the broad “arm” like structure at the top of the NGC 1084 image in Fig. 23.) The refractor observations were undertaken in order to confirm that our 0.7-m data are not compromised by scattered light. Our observations are not able to confirm the extended low surface brightness profiles reported in Merritt et al. (2016).

Finally, Fig. A1 in the Appendix present images of galaxies included in our study, along with scale bars for apparent and physical diameter. We include several figures here, with the rest included as supplemental material. The entire set of images will also be posted on the *HERON* website at IRSA.

Noting that a significant fraction of edge-on disk galaxies exhibit disturbances (e.g. NGC 3628 and NGC 4216), we suspect that the faintest detectable light at the edges of face-on disks in disk galaxies should be attributed to the disk, not the halo. Fig. 24 illustrates NGC 891, a typical edge-on galaxy with a bulge. The deepest exposures show that the outermost isophotes are trapezoidal, with the major axis aligned with the disk. Among the most striking examples of an edge-on trapezoidal envelope is NGC 2683. The minor axis is always aligned with the spheroidal component and perpendicular to the disk. This is characteristic of all of our edge-on disk galaxies: we have no cases where a low surface brightness envelope ever projects to a larger size than the disk, save for that M104. M104 can be considered a disk galaxy, showing a prominent dust lane and bulge, but does show one of the largest halos in our sample.

Fig. 25 shows the unusual case of NGC 3628. Although the tidal tail has long been noted, the buckled and disturbed disk is thick, with the deepest isophotes showing a boxy 2:1

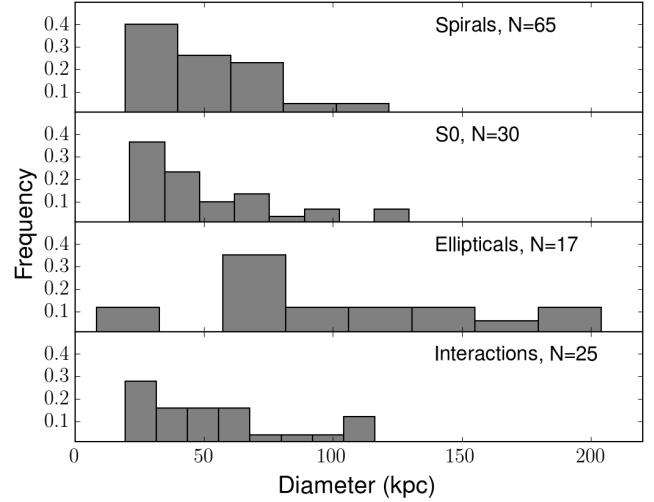


Figure 19. A set of histograms displaying the number of galaxies as a function of envelope diameter (kpc), separated by Hubble type. We can see that spiral and S0 galaxies are, in general, smaller than elliptical galaxies in our sample. The “interactions” histogram displays the envelope diameters of galaxies in our sample that show signs of interaction; such features include streams, plumes, or shells.

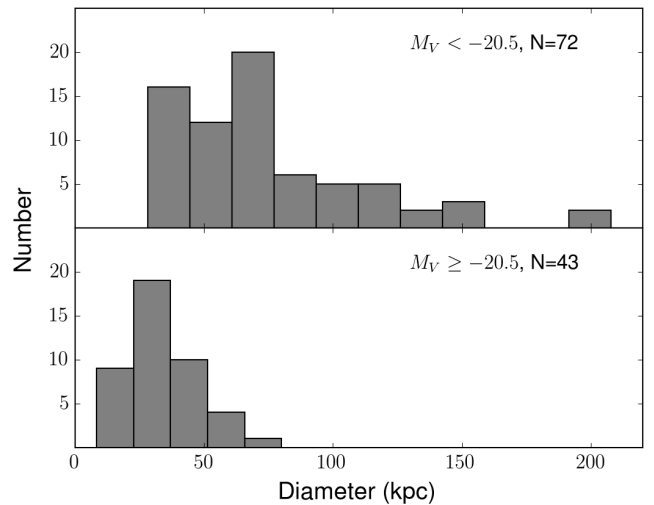


Figure 20. Histograms displaying the number of galaxies as a function of envelope diameter (kpc), divided by absolute magnitude at $M_V = -20.5$. It is clear that galaxies with $M_V < -20.5$ have a greater envelope diameter.

structure. One could safely assume that all light contributing to the low surface brightness components of this galaxy belongs to the disk. Fig. 26 shows the disturbed edge-on S0 galaxy NGC 4762. Deep images have previously shown the disturbed disk in the second panel, but our *HERON* images show an extended “shoe”-like structure that we suggest may consist of disk stars that were heated or disturbed during an interaction.

We conclude that the outermost detectable envelopes of face-on disks consist of disk stars. This position is based on Fig. 22, our deep imaging of edge-on disks in Figs. 24-

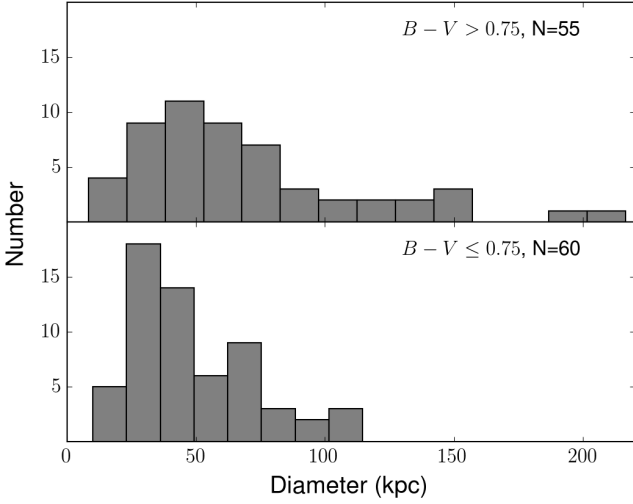


Figure 21. Another illustration that the largest halos are found at the bright end of the red sequence (Fig. 18). Histograms displaying the number of galaxies as a function of envelope diameter (kpc), divided by colour at $B - V = 0.75$. This represents a rough colour cut between the red sequence and blue cloud.

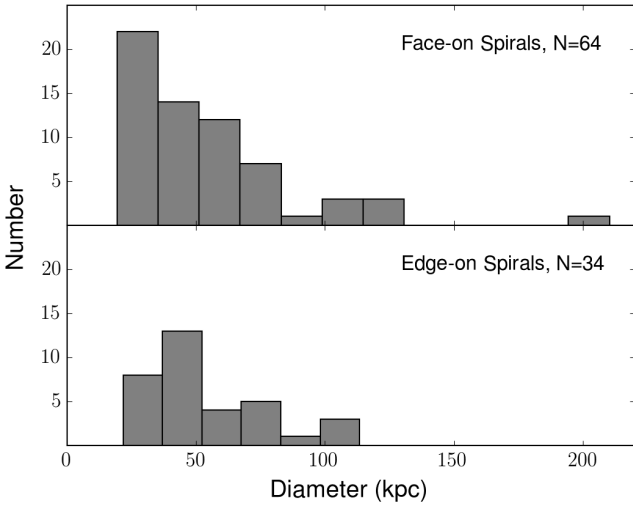


Figure 22. Envelope diameter for face-on and edge-on spirals. The KS-test gives $\mathcal{D} = 0.15$ and a p-value $\mathcal{P} = 0.62$ for this result. We do not find strong evidence for different diameters for edge-on versus face-on disks.

26, and the edge-on disks in our sample from A1 (including additional supplemental inverse images). Furthermore, deep HI images (e.g. Sancisi et al. 2008 and other studies) find HI envelopes around spiral galaxies in the disk plane, including that of M51. We argue that studies of face-on disk galaxies such as that of Merritt et al. (2016) are in fact detecting extended disk light. Fig. 23 illustrates our model subtractions of 3 of the galaxies in Merritt et al. (2016), and in all cases, spiral structure or disturbances dominate the outermost isophotes. Even though Merritt et al. (2016) finds light outside these isophotes, we are not able to extend our surface brightness measurements to such a faint level. Even so, we argue that for all disk galaxies, especially those with

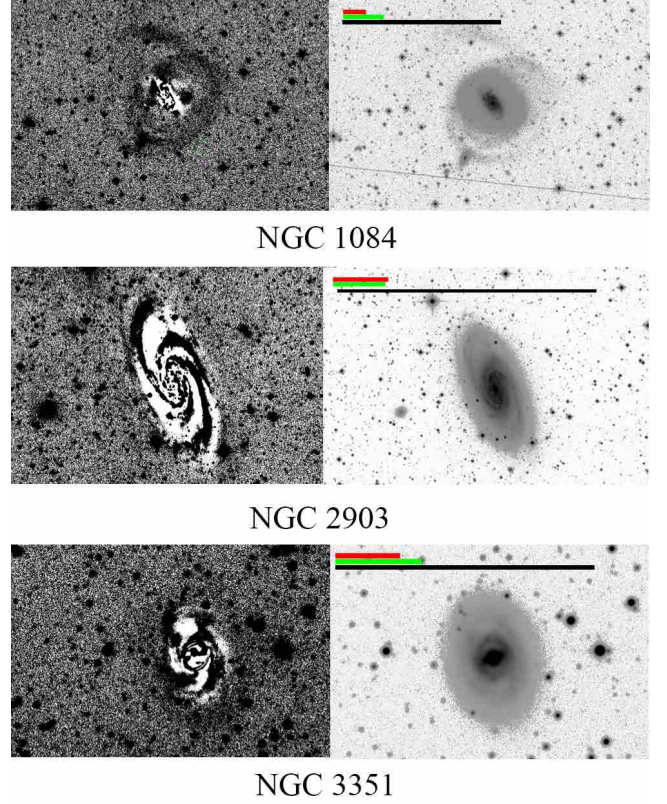


Figure 23. Subtraction images next to the corresponding inverse image. The black scale bar on the inverse image panels represents the diameter at the 30th mag/arcsec² that Merritt et al. (2016) lists in their paper. The green bar represents 5' and the red bar represents 10 kpc.

near face-on inclination, the lines of evidence from our stellar imaging study and that of Sancisi et al. (2008) and similar HI studies, support the outermost visible light isophotes being dominated by stars in the disk plane, not in the spheroidal old halo. These stars may owe their presence to disk flaring. Other evidence arises from studies of the extreme UV (XUV) disks e.g. Werk et al. (2010). Lemonias et al. (2011) found that 4-14% of galaxies to $z = 0.05$ have XUV disks, with 7-18% of galaxies in the green valley being candidates to transition away from the red sequence.

The prima facie evidence of a true Population II halo would be the presence of globular clusters, but detection of globular clusters in sufficient numbers at radii > 30 kpc would be difficult even if the spatial resolution were available to resolve them: distant clusters are rare, even in highly populated systems.

6 CONCLUSION

We report new imaging to low surface brightness for a sample of nearby galaxies predominantly from the 2MASS nearby bright galaxy catalogue, and mostly lying within the boundary of the Local Volume ~ 50 Mpc. We show that our imaging using the Jeanne Rich C28 0.7-m telescope reaches ~ 28 mag/arcsec², and reproduces well the low sur-

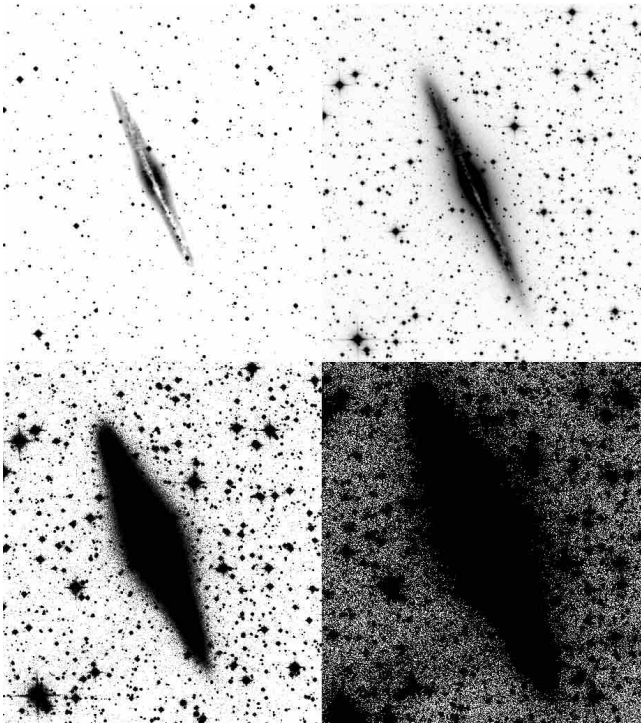


Figure 24. The edge-on spiral galaxy NGC 891 is displayed from shallow to deep stretch. Notice that the minor axis of the bulge is significantly smaller than the extent of the disk major axis; this is typical of all edge-on disk galaxies. At the deepest stretch, the galaxy assumes a “trapezoidal” appearance due to the extent of the spheroid, but the disk always has the greatest major axis.

face brightness structures and surface brightness profiles reported in the literature. In \sim one hour exposures, we reproduce published faint structure from amateur exposures of tens of hours, Dragonfly, and the CFHT. We did not fail to measure, or observe, any low surface brightness features reported by others in the literature.

We measure the diameters of the envelopes not including transient structures such as streams, arcs, and interaction filaments. We find a strong primary correlation between envelope diameter and M_V , after carefully checking for spurious correlations between envelope diameter and apparent surface brightness, and distance. We find that the largest envelopes are hosted by the most luminous elliptical galaxies. However, very large envelopes are found spanning the full range of morphological types, in the most luminous galaxies.

We consider our sample in the colour–magnitude diagram. While the largest envelopes are found in all parts of the CMD, the envelopes with $D > 100$ kpc are almost always found on the bright end of the red sequence, with $M_V < -21$ in E/S0 galaxies. The largest envelopes, those with $D > 40$ kpc, are only found in galaxies with $M_V < -20$; however 80% of the envelopes with $D > 60$ kpc are on the bright end of the red sequence. We find that interactions can occur with equal likelihood across the CMD, even on the red sequence. Although we can observe signs of interactions in the last 1-2 Gyr, these are not necessarily playing a role in

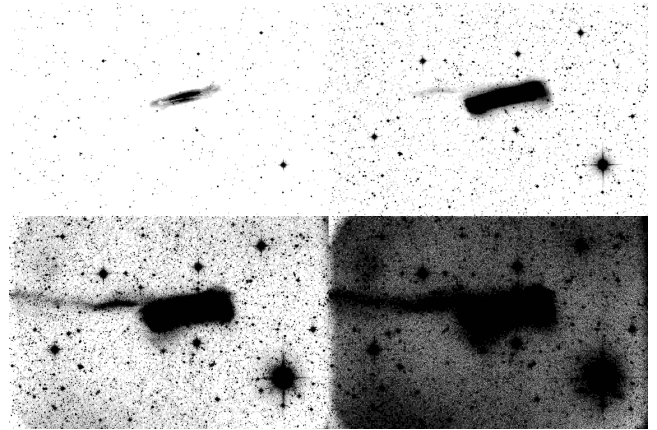


Figure 25. NGC 3628 is displayed from shallow to deep stretch. Notice that the disk grows from roughly normal in appearance to an almost rectangular morphology. This kind of disturbance may give rise to “rectangular” envelopes seen in some S0 galaxies, like that found in NGC 720. The thickness of the rectangular disk exceeds 50 kpc.

quenching of star formation. However, this question deserves more exploration, potentially in a future *HERON* project.

It is noteworthy to emphasize that it is mostly the total intrinsic luminosity, and *not* presence on the red sequence, that determines envelope diameter. Galaxies at the faint ends ($M_V > -21$) of the blue and red sequences have the same distribution of envelope sizes. While presence on the red sequence may have resulted from an early interaction history, the present-day absolute luminosity appears to be the critical factor that determines the size of the low surface brightness envelope.

We consider disk galaxies, and find that edge-on spirals have larger diameters than face-on spirals. We develop several lines of argument that the envelopes of disk galaxies are dominated by stars on the disk plane. We show that in the sample of Merritt et al. (2016) that the outermost portions of disks are dominated by spiral structure. We also illustrate two cases, NGC 4762 and NGC 3628, where interactions have resulted in the disk outskirts being strongly disturbed and thickened. Appealing to the HI imaging of Sancisi et al. (2008) and studies of XUV disks (Lemonias et al. 2011), we argue that the envelopes of disks are dominated by disk stars, not by the classical halo spheroid. The low surface brightness structures of all edge-on galaxies are dominated by their disks; there are no cases where the greatest diameter at low surface brightness arises from a classical spheroidal structure.

Future *HERON* work amongst an international team of observational and theoretical collaborators will report the quantitative analysis of surface brightness profiles, discuss outer envelope morphologies, and other properties including comparisons of extended structures in multiple wavelengths. We will also report and catalogue all low surface brightness companions detected in our survey, listing luminosities, diameters, and coordinates among other details. Finally, we will upload our complete datasets and imaging to the *HERON* archive at the IRSA/IPAC database.

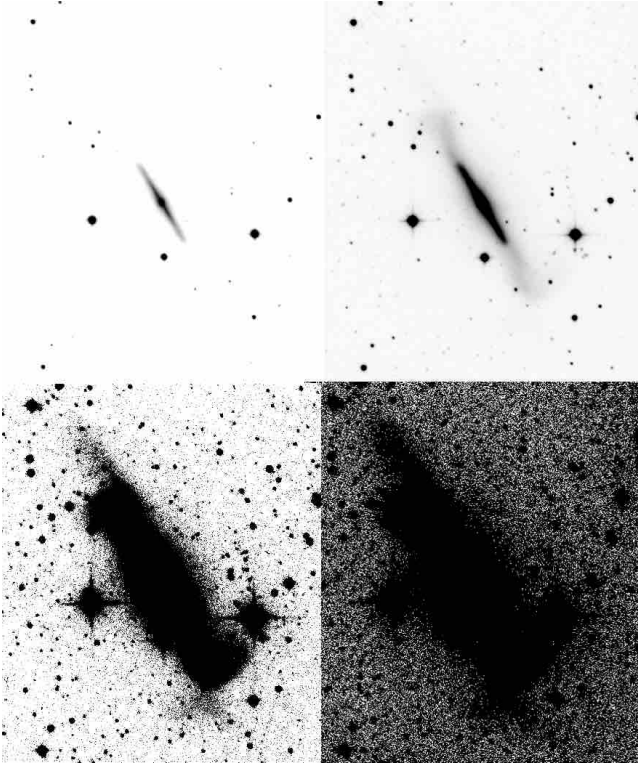


Figure 26. Extreme disturbance of the S0 NGC 4762, displayed with a range of stretch. The shallow exposures follow those in the Hubble Atlas of Galaxies, while the deepest stretch shows an almost “shoe”-like structure resulting from the interaction envelope.

ACKNOWLEDGEMENTS

The authors express thanks to Eija Laurikannen and Sebastien Comeron for valuable comments on the project. We would like to thank UCLA alumnus Kyra Mitchell for her valuable help creating our catalogue of inverse image grids, several of which are displayed in the Appendix with the rest included as supplemental materials (Fig. A1). We acknowledge UCLA alumnus Dylan Schaul, who worked on data reduction for the early images. We also acknowledge Nanjing University (Jiangsu Province, China) students Xu Zizheng and Weigong Cao for their help creating an image reduction pipeline which will be used in our future work. We also thank David Gedalia for his assistance in improvements of the 0.7-m Lockwood Valley telescope, and B. Megdal for his assistance in obtaining images using his 8-inch refractor. We also acknowledge Ian Kearns-Brown for technical and IT support of the Jeanne Rich telescope. We also thank the membership of the Polaris Observatory Association for their maintenance of the observatory infrastructure. Aleksandr Mosenkov expresses gratitude for the grant of the Russian Foundation for Basic Researches number mol_a 18-32-00194.

This research has made use of the NASA/IPAC Infrared Science Archive (IRSA; <http://irsa.ipac.caltech.edu/frontpage/>), and the NASA/IPAC Extragalactic Database (NED; <https://ned.ipac.caltech.edu/>), both of which are operated by the Jet Propulsion Laboratory, Califor-

nia Institute of Technology, under contract with the National Aeronautics and Space Administration. This research has made use of the HyperLEDA database (<http://leda.univ-lyon1.fr/>; Makarov et al. 2014).

Software: IRAF, IMSURFIT, Ellipse, DS9, Python, Veusz Graphing, Microsoft Excel.

REFERENCES

- Abraham, R. & van Dokkum, P., 2015 ApJ 782, L24
- Ahn C. P., et al., 2014, ApJS, 211, 17
- Agertz O., Kravtsov A. V., 2016, ApJ, 824, 79
- Amorisco, N. C. 2017, MNRAS, 469, L48
- Arp, H., & Bertola, F. 1969, *Astrophys. Lett.*, 4, 23
- Atkinson, A.M., Abraham, R.G., & Ferguson, A.M.N. ApJ, 765, 28
- Bechtol, K., Drlica-Wagner, A., Balbinot, E., et al. 2015, ApJ, 807, 50
- Behroozi P. S., Wechsler R. H., Wu H.-Y., Busha M. T., Klypin A. A., Primack J. R., 2013, ApJ, 763, 18
- Bell, E.F., McIntosh, D.H., Katz, N., Weinberg, M.D. 2003, ApJS, 149, 289
- Bellazzini, M., Cacciari, C., Federici, L., Fusi Pecci, F., & Rich, M. 2003, A&A, 405, 867
- Belokurov, V., Zucker, D. B., Evans, N. W., et al. 2006, ApJ, 642, L137
- Belokurov, V., Evans, N. W., Irwin, M. J., et al. 2007, ApJ, 658, 337
- Belokurov, V., Zucker, D. B., Evans, N. W., et al. 2007, ApJ, 654, 897
- Bertin, E., & Arnouts, S. 1996, A&AS, 117, 393
- Binggeli, B., Sandage, A., & Tammann, G. A. 1988, ARA&A, 26, 509
- Blauensteiner, M., Rempel, P., Riepe, P., et al. 2017, *Astrophysics*, 60, 295
- Boylan-Kolchin, M., Bullock, J. S., & Kaplinghat, M. 2012, MNRAS, 422, 1203
- Boylan-Kolchin, M., Bullock, J. S., & Kaplinghat, M. 2011, MNRAS, 415, L40
- Brosch, N., Polishook, D., Shporer, A., et al. 2008, Ap&SS, 314, 163
- Brosch, N. 2015, MNRAS, 454, 3222
- Brosch, N., Kaspi, S., Niv, S. & Manulis, I. 2015 Ap&SS 359, 49
- Brosch, N., Koriski, S., Rich, R. M., & Mosenkov, A. V. 2019, MNRAS, 482, 2284
- Brown, T. M., Ferguson, H. C., Smith, E., et al. 2003, ApJ, 592, L17
- Brown, T. M., Smith, E., Ferguson, H. C., et al. 2006, ApJ, 652, 323
- Bullock, J. S., Kravtsov, A. V., & Weinberg, D. H. 2000, ApJ, 539, 517
- Bullock, J. S., Kravtsov, A. V., & Weinberg, D. H. 2001, ApJ, 548, 33
- Bullock, J. S., & Johnston, K. V. 2005, ApJ, 635, 931
- Bureau M., Freeman K. C., 1999, AJ, 118, 126
- Chambers K. C., et al., 2016, arXiv e-prints, arXiv:1612.05560
- Cole, S., Lacey, C. G., Baugh, C. M., & Frenk, C. S. 2000, MNRAS, 319, 168
- Cooper, A. P., Cole, S., Frenk, C. S., et al. 2010, MNRAS, 406, 744
- Cooper, A. P., D'Souza, R., Kauffmann, G., et al. 2013, MNRAS, 434, 3348
- Cunningham, E. C., Deason, A. J., Guhathakurta, P., et al. 2016, ApJ, 820, 18
- de Vaucouleurs, G. 1969, *Astrophys. Lett.*, 4, 17
- Di Cintio, A., Brook, C. B., Macciò, A. V., et al. 2014, MNRAS, 437, 415
- Duc, P.-A., Cuillandre, J.-C., Karabal, E., et al. 2015, MNRAS, 446, 120
- Duc, P.-A., 2017, IAU Symp. 321, 180
- Duc, P. A., Cuillandre, J.-C., & Renaud, F. 2018, MNRAS, 475, L40
- Durrell, P.R., Harris, W.E., & Pritchett, C.J. 2001, AJ, 121, 2557
- Elias L. M., Sales L. V., Creasey P., Cooper M. C., Bullock J. S., Rich M. R., Hernquist L. 2018, MNRAS, 479, 4004
- Fakhouri, O., Ma, C.-P., & Boylan-Kolchin, M. 2010, MNRAS, 406, 2267
- Ferguson, H. C., & Sandage, A. 1989, ApJ, 346, L53
- Ferrarese, L. et al. 2006 ApJS 164, 334
- Finkbeiner, D. P., Schlafly, E. F., Schlegel, D. J., et al. 2016, ApJ, 822, 66
- Flewelling H. A., et al., 2016, arXiv e-prints, arXiv:1612.05243
- Gaia Collaboration, et al., 2016, A&A, 595, A1
- Gaia Collaboration, et al., 2018, A&A, 616, A1
- Garrison-Kimmel, S., Wetzel, A., Bullock, J. S., et al. 2017, MNRAS, 471, 1709
- Garrison-Kimmel, S., Bullock, J. S., Boylan-Kolchin, M., & Bardwell, E. 2017, MNRAS, 464, 3108
- Governato, F., Brook, C., Mayer, L., et al. 2010, Nature, 463, 203
- Green G. M., Schlafly E. F., Zucker C., Speagle J. S., Finkbeiner D. P., 2019, arXiv e-prints, arXiv:1905.02734
- Harmen, B.; Monachesi, A.; Bell, E. F.; de Jong, R. S.; Bailin, J.; Radburn-Smith, D. J. & Holwerda, B. W. 2017, MNRAS, 466, 1491
- Hood, C.E. Kannappan, S.J. Stark, D.V., Dell'Antonio, I.P., Moffett, A.J., Eckert, K.D., Norris, M.A., & Hendel, D. 2018, ApJ, 857, 144
- Ibata R. A., et al., 2013, Natur, 493, 62
- Jarrett, T.H. et al. 2003 AJ 125, 525
- Javanmardi, B., Martinez-Delgado, D., Kroupa, P., et al. 2016, A&A, 588, A89
- Johnston, K. V. 1998, ApJ, 495, 297
- Karabal E., Duc P.-A., Kuntschner H., Chanial P., Cuillandre J.-C., Gwyn S., 2017, A&A, 601, A86
- Karachentsev I. D., 1965, Ap, 1, 118
- Karachentsev, I. D., Makarova, L. N., Tully, R. B., et al. 2017, MNRAS, 469, L113
- Kazantzidis, S., Bullock, J. S., Zentner, A. R., Kravtsov, A. V., & Moustakas, L. A. 2008, ApJ, 688, 254-276
- Koch, A., Rich, R. M., Reitzel, D. B., et al. 2008, ApJ, 689, 958-982
- Koch, A. et al. 2012 ApJ 755, L13
- Koch, A., Black, C. S., Rich, R. M., et al. 2017, *Astronomische Nachrichten*, 338, 503
- Klypin, A., Kravtsov, A. V., Valenzuela, O., & Prada, F. 1999, ApJ, 522, 82
- Kormendy, J., & Bahcall, J. N. 1974, AJ, 79, 671
- Kormendy, J., Fisher, D. B., Cornell, M. E., & Bender, R. 2009, ApJS, 182, 216
- Lemonias, J. J., Schiminovich, D., Thilker, D., et al. 2011, ApJ, 733, 74
- Lundmark, K. 1920, *Kungl. Svenska Vetenskapsakademiens Handlingar*, 60, 1
- Mackey, A. D., Kuposov, S. E., Erkal, D., et al. 2016, MNRAS, 459, 239
- Makarov, D., Prugniel, P., Terekhova, N., Courtois, H., & Vauglin, I. 2014, A&A, 570, A13
- Malin, D. F. 1978, Nature, 276, 591
- Malin D. F., 1979, Natur, 277, 279
- Malin, D. F., & Carter, D. 1980, Nature, 285, 643
- Martínez-Delgado, D., Gabany, R. J., Crawford, K., et al. 2010, AJ, 140, 962
- Martínez-Delgado, D., Romanowsky, A. J., Gabany, R. J., et al. 2012, ApJ, 748, L24
- McConnachie, A. W., Irwin, M. J., Ibata, R. A., et al. 2009, Nature, 461, 66
- Malin D., Hadley B., 1997, ASPC, 116, 460
- Merritt, A., van Dokkum, P., Abraham, R., & Zhang, J. 2016, ApJ, 830, 62
- Mihos, J. C., Harding, P., Feldmeier, J., & Morrison, H. 2005, ApJ, 631, L41
- Mihos, J. C., Harding, P., Feldmeier, J. J., et al. 2017, ApJ, 834, 16

- Miskolczi, A., Bomans, D. J., & Dettmar, R.-J. 2011, *A&A*, 536, A66
- Misgeld, I., & Hilker, M. 2011 *MNRAS* 414 3699
- Monachesi A., Bell E. F., Radburn-Smith D. J., Bailin J., de Jong R. S., Holwerda B., Streich D., Silverstein G., 2016, *MNRAS*, 457, 1419
- Moore, B., Ghigna, S., Governato, F., et al. 1999, *ApJ*, 524, L19
- Morales G., Martínez-Delgado D., Grebel E. K., Cooper A. P., Javanmardi B., Miskolczi A., 2018, *Å*, 614, A143
- Mori, M., & Rich, R. M. 2008, *ApJ*, 674, L77
- Mouhcine, M., Ferguson, H. C., Rich, R. M., Brown, T. M., & Smith, T. E. 2005, *ApJ*, 633, 821
- Müller O., et al., 2019, *Å*, 624, L6
- Muñoz-Mateos, J.C., Sheth, K., Regan, M., Kim, T., Laine, J., Erroz-Ferrer, S., Gil de Paz, A. Comeron, S., Hinz, J., Laurikainen, E. et al. 2015 *ApJS*, 219, 3
- Muslimov, E., Valls-Gabaud, D., Lemaître, G., et al. 2017, *arXiv:1710.08776*
- Paudel, S., & Ree, C. H. 2014, *ApJ*, 796, L14
- Pease, F. G. 1920, *ApJ*, 51,
- Peng C. Y., Ho L. C., Impey C. D., Rix H.-W., 2002, *AJ*, 124, 266
- Peng C. Y., Ho L. C., Impey C. D., Rix H.-W., 2010, *AJ*, 139, 2097
- Pillepich, A., Madau, P., & Mayer, L. 2015, *ApJ*, 799, 184
- Purcell, C. W., Bullock, J. S., & Kazantzidis, S. 2010, *MNRAS*, 404, 1711
- Read J. I., Iorio G., Agertz O., Fraternali F., 2017, *MNRAS*, 467, 2019
- Rich, R. M., Mighell, K. J., Freedman, W. L., & Neill, J. D. 1996, *AJ*, 111, 768
- Rich, R.M. et al. 2012, *Nature* 482, 192
- Rich, R. M., Brosch, N., Bullock, J., et al. 2017, *Formation and Evolution of Galaxy Outskirts*, 321, 186
- Sancisi R., Fraternali F., Oosterloo T., van der Hulst T., 2008, *A&ARv*, 15, 189
- Sandin, C. 2014, *A&A*, 567, A97
- Sandin, C. 2015, *A&A*, 577, A106
- Schlafly, E. F., & Finkbeiner, D. P. 2011, *ApJ*, 737, 103
- Sérsic, J. L. 1968, *Atlas de Galaxias Australes*
- Shi D. D., et al., 2017, *ApJ*, 846, 26
- Stewart, K. R., Bullock, J. S., Wechsler, R. H., Maller, A. H., & Zentner, A. R. 2008, *ApJ*, 683, 597-610
- Tal, T., van Dokkum, P. G., Nelan, J., & Bezanson, R. 2009, *AJ*, 138, 1417
- Trujillo, I., & Fliri, J. 2016, *ApJ*, 823, 123
- Tully, R. B., Courtois, H. M., & Sorce, J. G. 2016, *AJ*, 152, 50
- van Dokkum, P. G., Abraham, R., & Merritt, A. 2014, *ApJ*, 782, L24
- van Dokkum, P. G., Abraham, R., Merritt, A., et al. 2015, *ApJ*, 798, L45
- Watkins, A. E., Mihos, J. C., & Harding, P. 2015, *ApJ*, 800, L3
- Werk J. K., et al., 2010, *AJ*, 139, 279
- Wetzel, A. R., Hopkins, P. F., Kim, J.-h., et al. 2016, *ApJ*, 827, L23
- White, D. J., Daw, E. J., & Dhillon, V. S. 2011, *Classical and Quantum Gravity*, 28, 085016
- Zhang, J., Abraham, R., van Dokkum, P., Merritt, A., Janssesen S. 2018, *ApJ*, 855, 78
- Zwicky, F. 1956, *Ergebnisse der exakten Naturwissenschaften*, 29, 344

APPENDIX A: HERON IMAGES**APPENDIX B: HERON TABLES**

This paper has been typeset from a $\text{\TeX}/\text{\LaTeX}$ file prepared by the author.

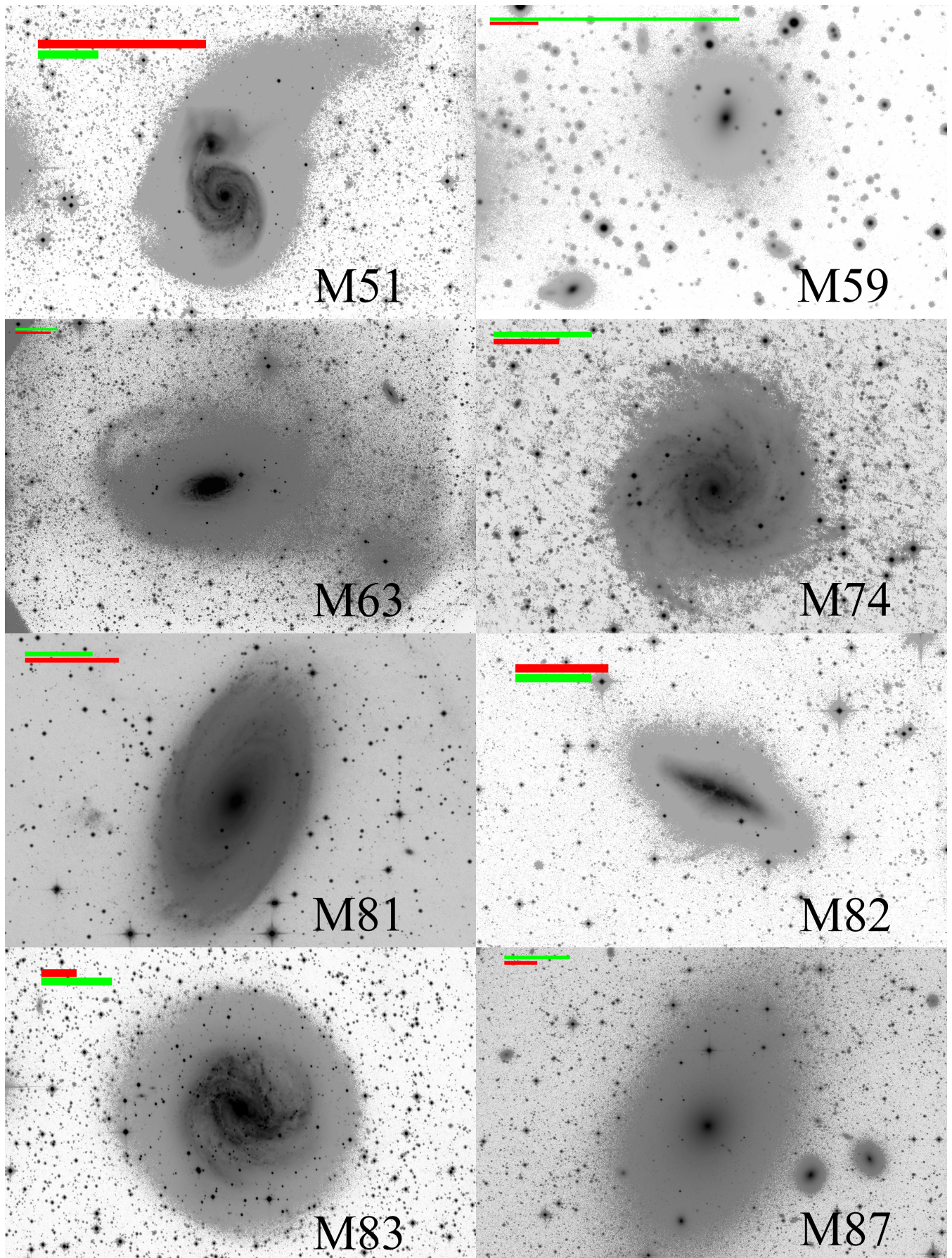
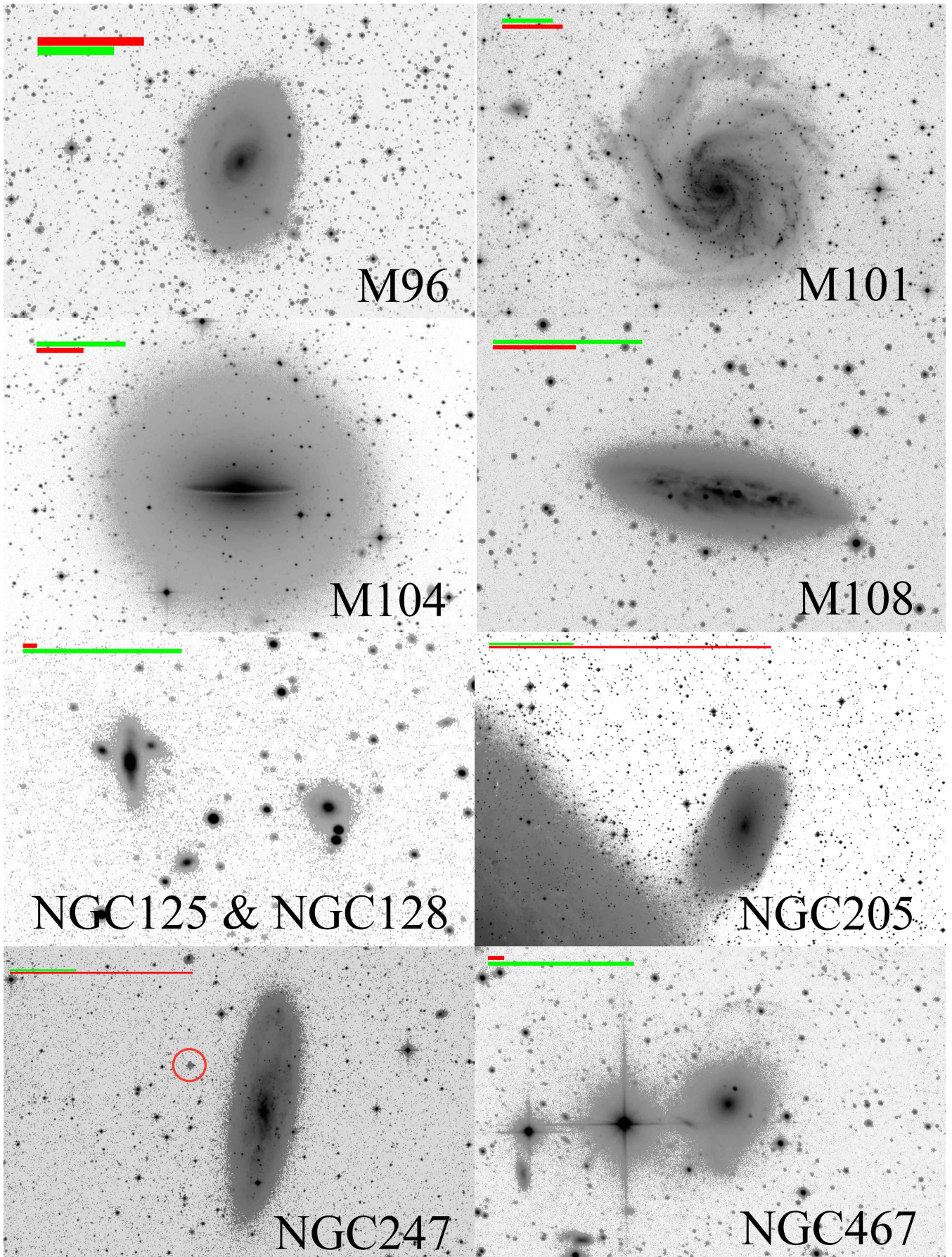


Figure A1. Inverse images of some galaxies from our sample. The green scale bar is 5'; the red scale bar is 10 kpc at the distance of the galaxy as listed in Table B. MNRAS 000, 1–19 (2018)



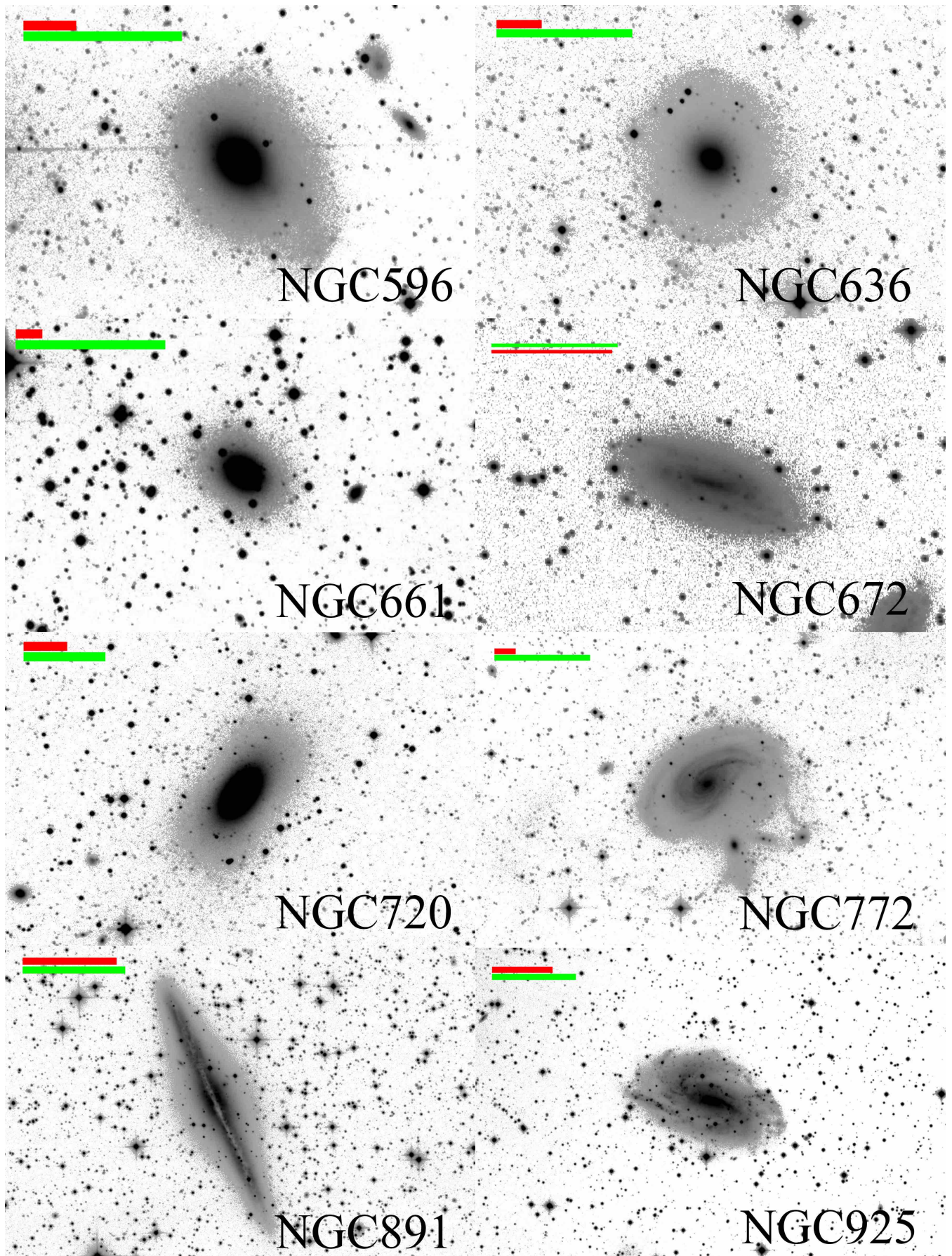
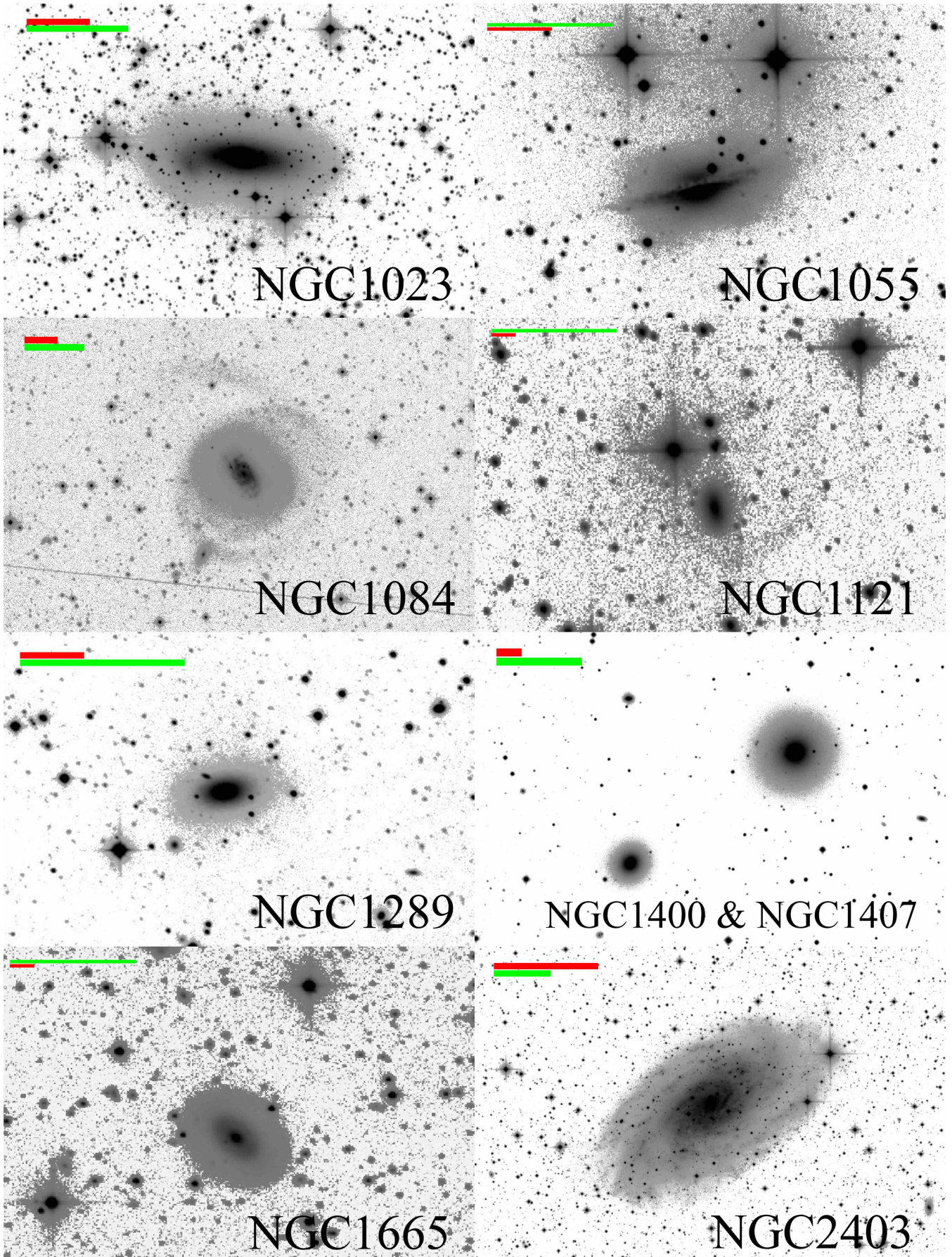


Figure A1. (continued)



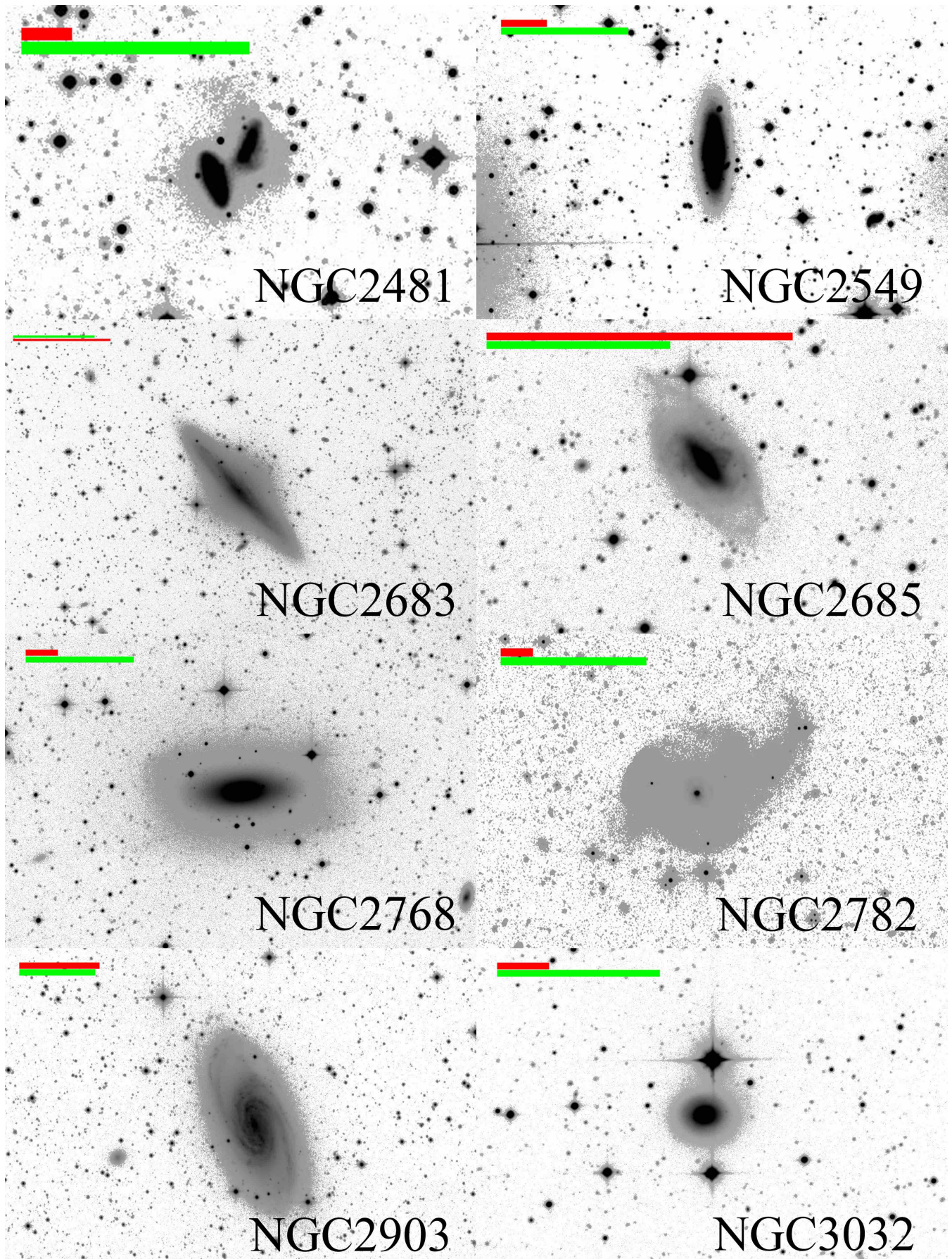
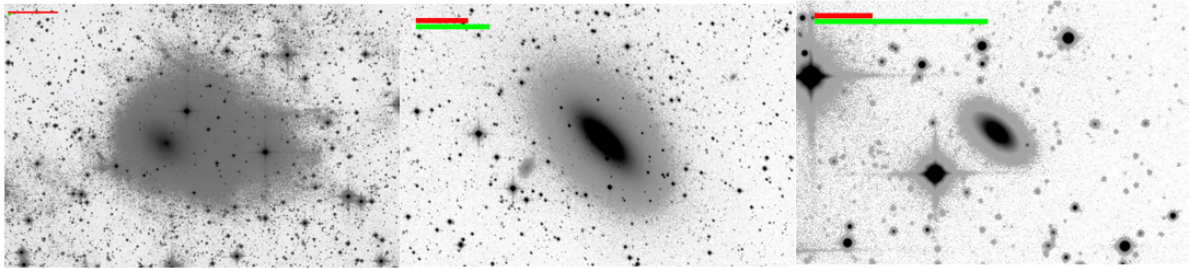


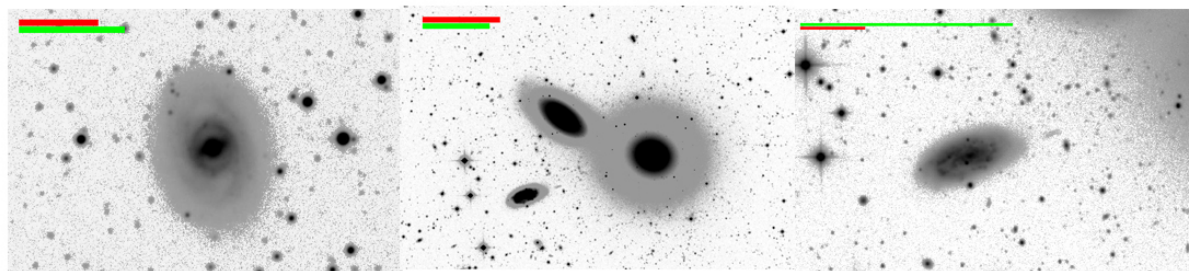
Figure A1. (continued)



NGC3077

NGC3115

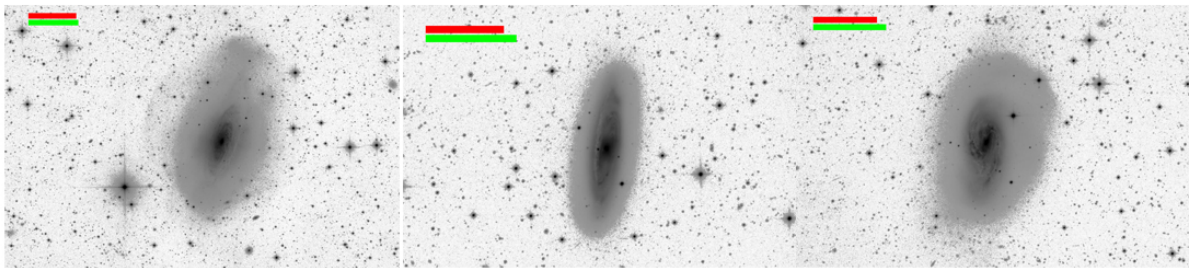
NGC3156



NGC3351

NGC3379 & 3384

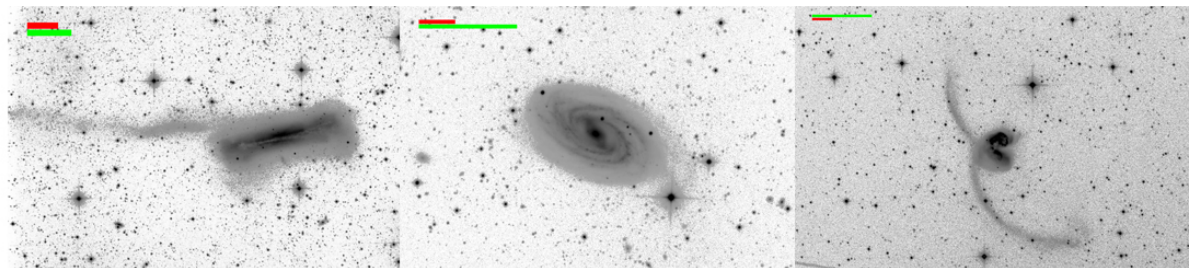
NGC3389



NGC3521

NGC3623

NGC3627

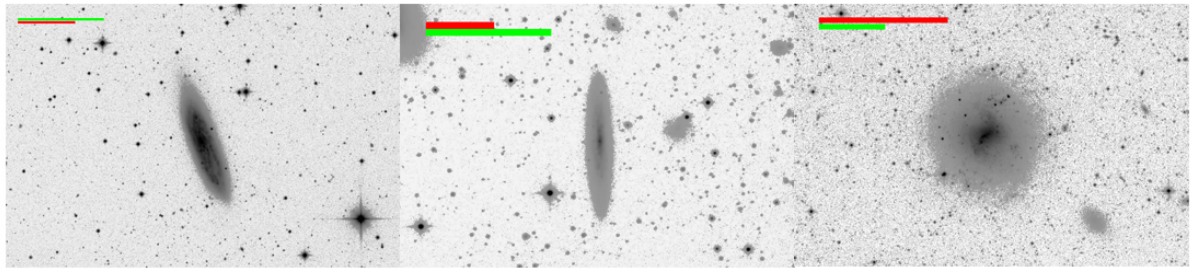


NGC3628

NGC3992

NGC4038

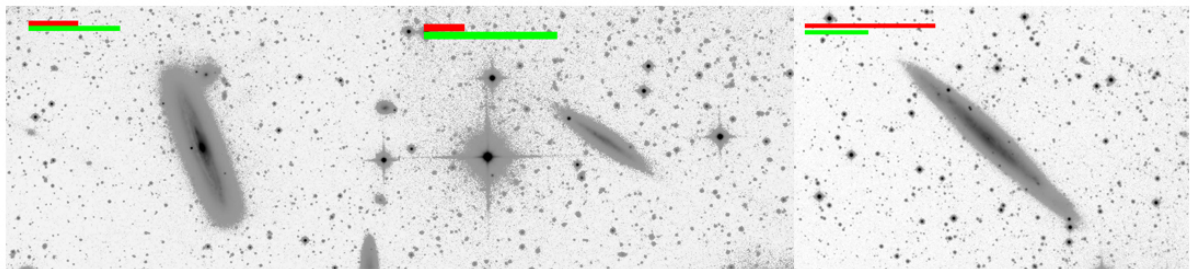
Figure A1. (continued)



NGC4096

NGC4206

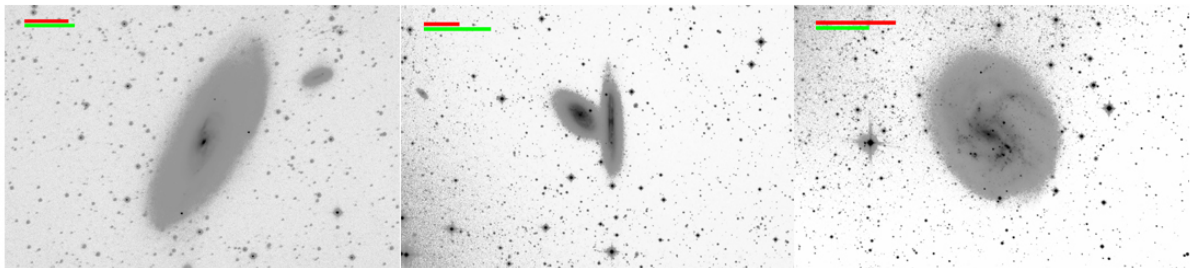
NGC4214



NGC4216

NGC4222

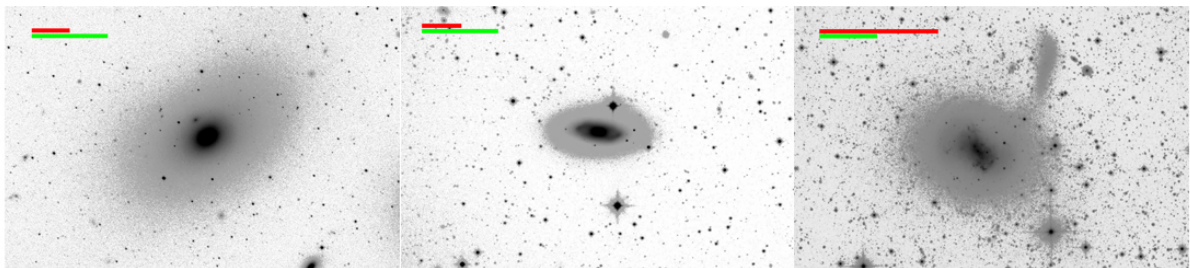
NGC4244



NGC4258

NGC4302

NGC4395

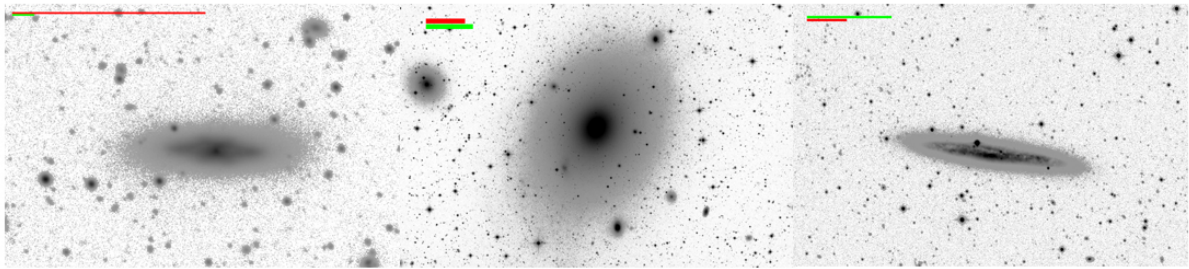


NGC4406

NGC4429

NGC4449

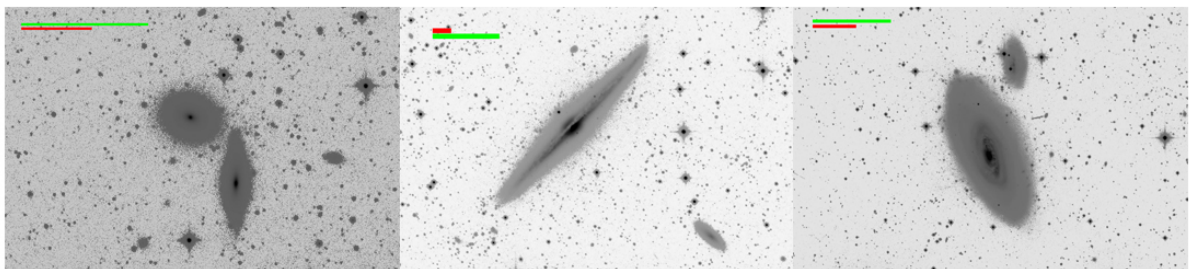
Figure A1. (continued)



NGC4469

NGC4472

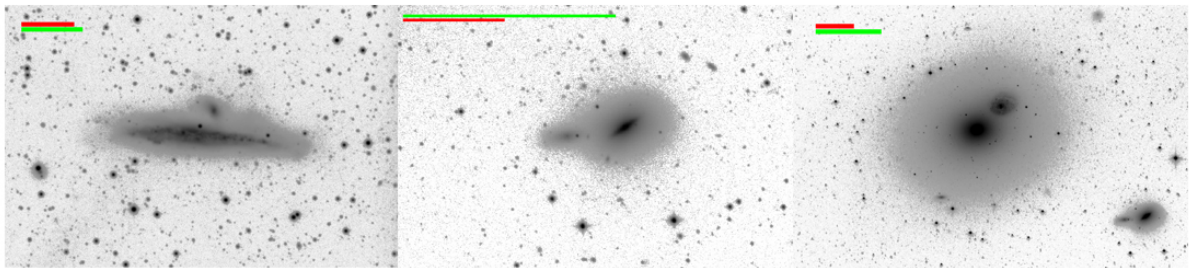
NGC4517



NGC4550

NGC4562 & 4565

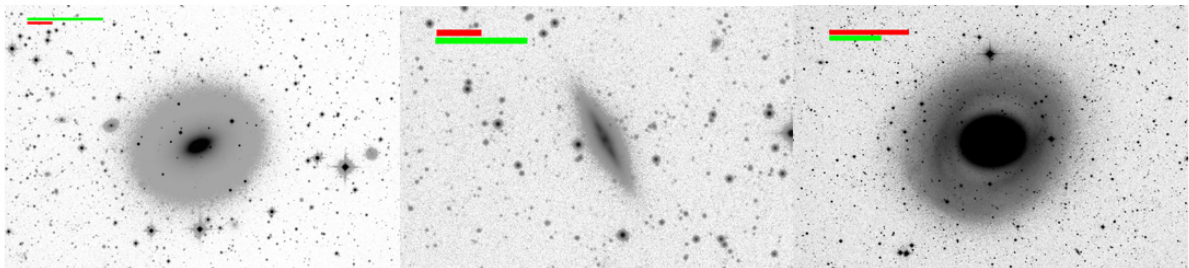
NGC4569



NGC4631

NGC4638

NGC4649

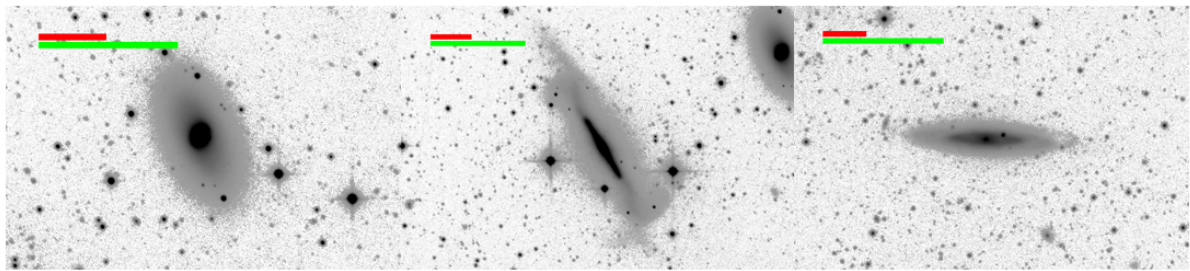


NGC4697

NGC4710

NGC4736

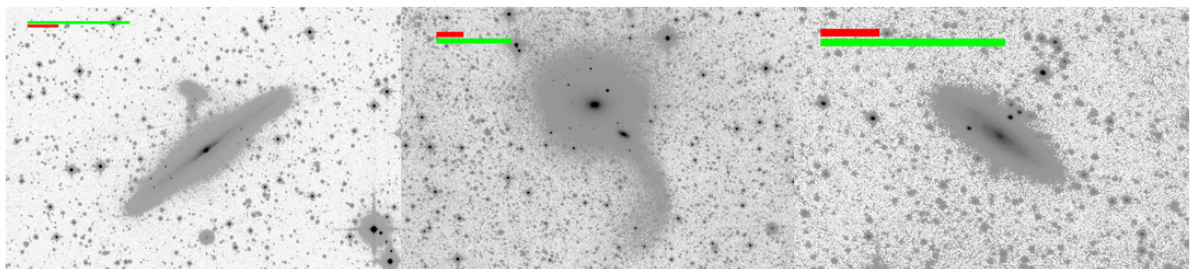
Figure A1. (continued)



NGC4754

NGC4762

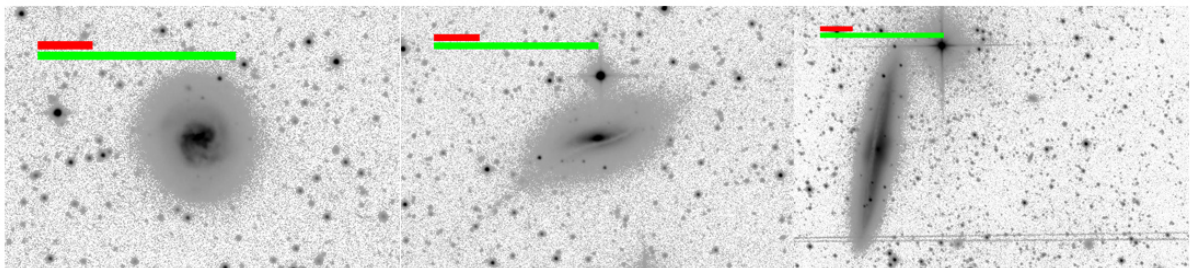
NGC4866



NGC5170

NGC5576

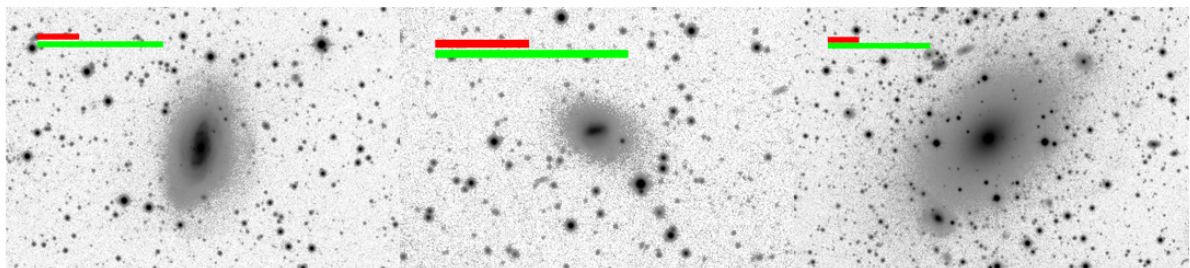
NGC5577



NGC5713

NGC5719

NGC5746

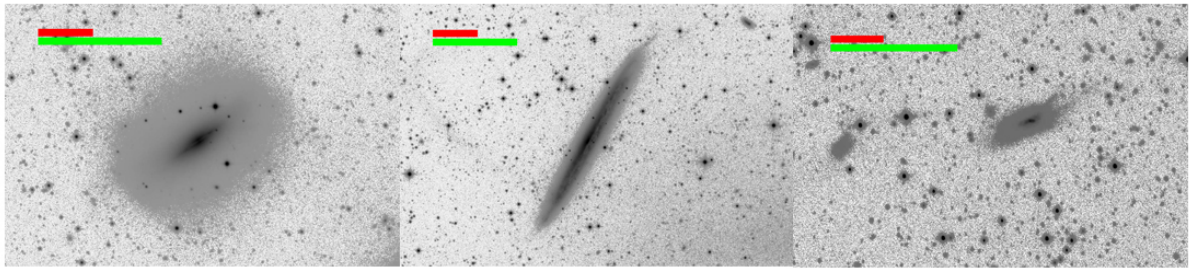


NGC5806

NGC5811

NGC5813

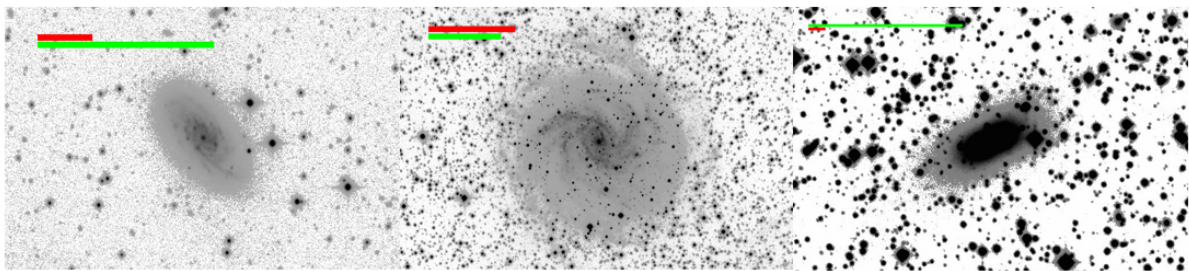
Figure A1. (continued)



NGC5866

NGC5907

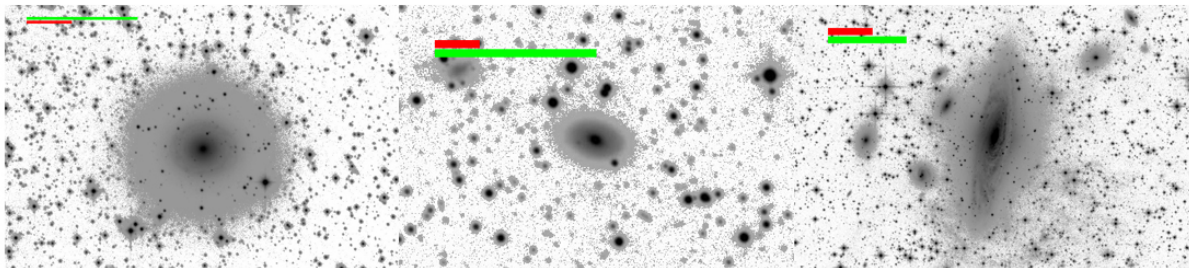
NGC6239



NGC6643

NGC6946

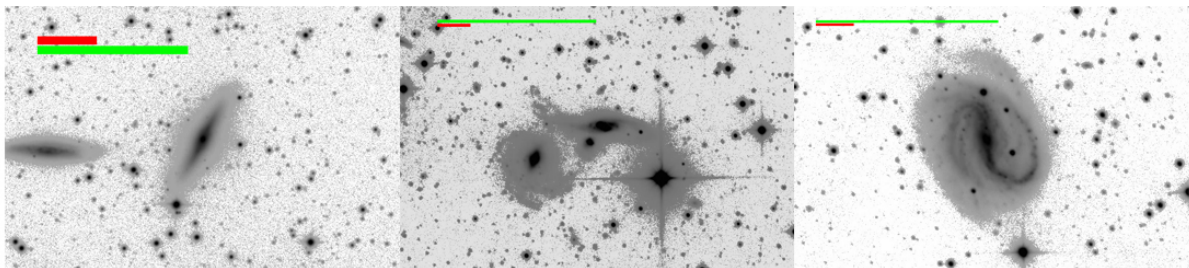
NGC7052



NGC7217

NGC7280

NGC7331

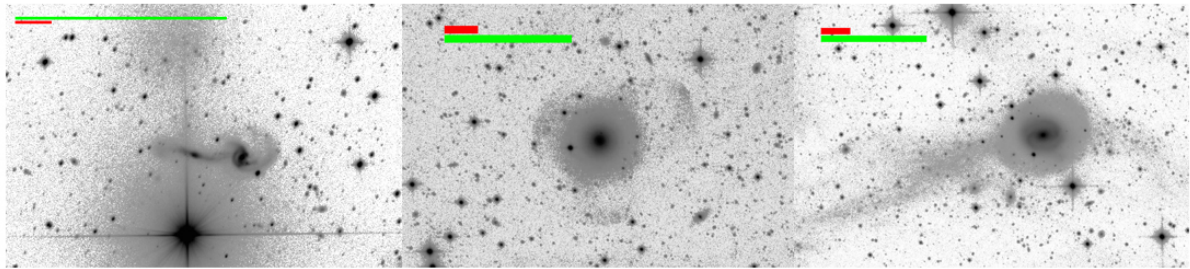


NGC7332

NGC7463

NGC7479

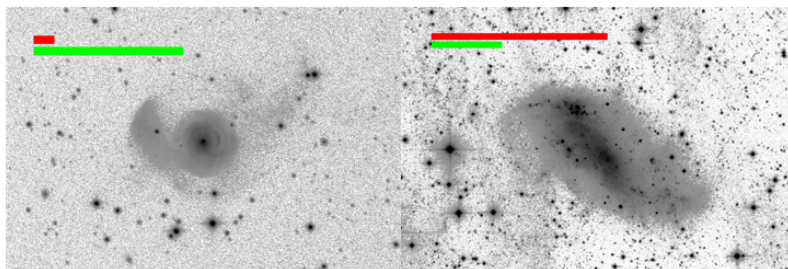
Figure A1. (continued)



NGC7741

NGC7742

NGC7743



UGC4872

UGC5666

Figure A1. (continued)

Table B1. Lists the coordinates (from HyperLeda), distance (see the text), radial velocity (from HyperLeda), type (from NED), apparent and absolute magnitude in the V band and the colour $B - V$ (using the HyperLeda values *btc* and *bvtc*). Also, in the column Features we note if a galaxy is viewed edge-on ('E') or interacting ('I').

NGC	RA, Dec hrs,degs	D Mpc	v km/s	Type	Features	m_V mag	M_V mag	$B - V$ mag
M49(4472)	12h29m46s +07h59m59s	16.63	978	E2/S0	...	8.32	-22.79	0.93
M51(5194/5195)	13h29m52s +47h11m42s	8.58	460	SA(s)bc	I	7.81	-21.86	0.55
M59(4621)	12h42m02s +11h38m50s	14.74	438	E5	...	9.54	-21.31	0.91
M60(4649)	12h43m39s +11h33m09s	17.05	1107	E2	I	8.74	-22.41	0.94
M63(5055)	13h15m49s +42h01m45s	9.04	507	SA(rs)bc	...	8.24	-21.54	0.66
M65(3623)	11h18m55s +13h05m32s	12.87	801	SAB(rs)a	...	8.81	-21.74	0.78
M66(3627)	11h20m15s +12h59m29s	11.46	718	SAB(s)b	...	8.47	-21.82	0.63
M74(628)	01h36m41s +15h47m00s	10.14	658	SA(s)c	...	8.91	-21.12	0.49
M81(3031)	09h55m33s +69h03m54s	3.60	-37	SA(s)ab	...	6.29	-21.49	0.83
M82(3034)	09h55m52s +69h40m47s	3.62	231	I0	E	7.07	-20.72	0.69
M83(5236)	13h37m00s -29h51m56s	4.90	508	SAB(s)c	...	6.95	-21.50	0.60
M86(4406)	12h26m11s +12h56m44s	17.39	-291	S0(3)/E3	...	8.72	-22.48	0.91
M87(4486)	12h30m49s +12h23m25s	16.78	1283	E+	...	8.62	-22.50	0.93
M90(4569)	12h36m49s +13h09m48s	11.86	-220	SAB(rs)ab	...	8.91	-21.46	0.61
M94(4736)	12h50m53s +41h07m13s	4.39	313	(R)SA(r)ab	...	7.83	-20.38	0.72
M95(3351)	10h43m57s +11h42m13s	9.93	777	SB(r)b	...	9.43	-20.55	0.73
M96(3368)	10h46m45s +11h49m11s	9.79	892	SAB(rs)ab	...	8.96	-21.00	0.80
M101(5457)	14h03m12s +54h20m56s	7.11	236	SAB(rs)cd	...	7.86	-21.40	0.44
M104(4594)	12h39m59s -11h37m22s	8.60	1087	SA(s)a	E	7.85	-21.82	0.88
M105(3379)	10h47m49s +12h34m53s	11.32	918	E1	I	9.19	-21.08	0.93
M106(4258)	12h18m57s +47h18m13s	7.61	454	SAB(s)bc	...	7.88	-21.53	0.60
M108(3556)	11h11m30s +55h40m27s	9.83	697	SB(s)cd	E	9.41	-20.56	0.57
M109(3992)	11h57m35s +53h22m28s	25.27	1047	SB(rs)bc	...	9.40	-22.61	0.71
M110(205)	00h40m22s +41h41m07s	0.80	-241	E5	...	7.87	-16.65	0.80
125	00h28m50s +02h50m20s	63.68	5273	(R)SA0+	...	12.24	-21.78	0.89
128	00h29m15s +02h51m50s	44.87	4129	S0	EI	11.58	-21.68	0.90
247	00h47m08s -20h45m37s	3.71	155	SAB(s)d	...	8.18	-19.67	0.44
278	00h52m04s +47h33m01s	17.78	639	SAB(rs)b	...	10.44	-20.81	0.51
467	01h19m10s +03h18m02s	58.61	5568	SA(s)0	I	11.98	-21.86	0.96
470	01h19m44s +03h24m35s	48.75	2373	SA(rs)b	I	11.38	-22.06	0.66
474	01h20m06s +03h24m55s	27.54	2342	(R')SA(s)0	I	11.42	-20.78	0.81
509	01h23m24s +09h26m00s	32.89	2273	S0	...	13.67	-18.91	0.74
518	01h24m17s +09h19m51s	38.73	2685	Sa	E	12.89	-20.05	0.74
520	01h24m35s +03h47m32s	17.86	2161	Sa	I	10.99	-20.27	0.70
524	01h24m47s +09h32m19s	32.58	2422	SA(rs)0+	...	10.11	-22.45	0.96
525	01h24m52s +09h42m11s	23.58	1624	S0	...	13.44	-18.42	0.75
530	01h24m41s -01h35m13s	71.81	5024	SB0+	E	12.61	-21.68	0.91
532	01h25m17s +09h15m50s	34.66	2369	SAb	E	12.30	-20.40	0.86
596	01h32m51s -07h01m53s	21.55	1903	E+	...	10.83	-20.83	0.85
636	01h39m06s -07h30m45s	29.47	1854	E3	...	11.32	-21.03	0.91
661	01h44m14s +28h42m21s	37.15	3817	E+	...	11.99	-20.86	0.88
672	01h47m53s +27h25m55s	7.21	426	SB(s)cd	...	9.97	-19.32	0.43
720	01h53m00s -13h44m18s	27.38	1717	E5	...	10.10	-22.08	0.95
772	01h59m19s +19h00m27s	25.47	2460	SA(s)b	I	9.39	-22.64	0.65
891	02h22m33s +42h20m51s	9.85	527	SA(s)b	E	9.04	-20.93	0.71
925	02h27m16s +33h34m44s	9.20	553	SAB(s)d	...	9.38	-20.44	0.45
1023	02h40m23s +39h03m47s	9.56	645	SB(rs)0-	I	8.42	-21.49	0.92
1055	02h41m45s +00h26m36s	19.34	993	SBb	E	10.14	-21.30	0.72
1084	02h45m59s -07h34m42s	15.46	1422	SA(s)c	I	10.26	-20.69	0.51
1289	03h18m49s -01h58m23s	29.92	2835	SB(rs)0	...	12.34	-20.04	0.80
1400	03h39m30s -18h41m17s	26.06	589	SA0-	...	10.79	-21.29	0.90
1407	03h40m11s -18h34m49s	28.54	1791	E0	...	9.46	-22.82	0.95
2403	07h36m51s +65h36m08s	3.20	140	SAB(s)cd	...	7.78	-19.75	0.38
2481	07h57m13s +23h46m03s	31.72	2180	S0/a	I	12.32	-20.19	0.67
2549	08h18m58s +57h48m11s	12.51	1075	SA(r)0	E	11.01	-19.48	0.85
2683	08h52m41s +33h25m20s	9.38	420	SA(rs)b	E	8.37	-21.50	0.76
2685	08h55m34s +58h44m03s	12.65	877	(R)SB0+	I	11.16	-19.35	0.76
2768	09h11m37s +60h02m14s	22.15	1397	S0	...	9.71	-22.01	0.92
2782	09h14m05s +40h06m49s	16.98	2623	SAB(rs)a	I	11.50	-19.65	0.61
2903	09h32m10s +21h30m05s	9.32	555	SAB(rs)bc	...	8.28	-21.57	0.57
3032	09h52m08s +29h14m11s	20.00	1540	SAB(r)0	...	12.34	-19.16	0.64

Table B1 – *continued*

NGC	RA, Dec hrs,degs	<i>D</i> Mpc	<i>v</i> km/s	Type	Features	<i>m_V</i> mag	<i>M_V</i> mag	<i>B – V</i> mag
3079	10h01m58s +55h40m47s	16.52	1163	SB(s)c	E	9.45	-21.64	0.53
3115	10h05m13s -07h43m06s	9.65	648	S0-	E	9.00	-20.92	0.90
3156	10h12m41s +03h07m45s	22.15	1346	S0	...	12.21	-19.51	0.71
3384	10h48m16s +12h37m45s	9.42	563	SB(s)0-	I	9.90	-19.97	0.88
3389	10h48m27s +12h31m59s	19.32	1301	SA(s)c	...	11.42	-20.01	0.36
3521	11h05m48s +00h02m05s	12.39	801	SAB(rs)bc	...	8.55	-21.92	0.71
3628	11h20m16s +13h35m22s	10.82	845	SAb	E	8.49	-21.68	0.68
4038	12h01m53s -18h52m05s	24.49	1634	SB(s)m	I	9.82	-22.12	0.57
4096	12h06m01s +47h28m42s	11.99	563	SAB(rs)c	...	9.53	-20.87	0.50
4206	12h15m16s +13h01m26s	18.87	702	SA(s)bc	E	11.16	-20.22	0.50
4214	12h15m39s +36h19m35s	2.98	292	IAB(s)m	...	9.51	-17.86	0.41
4216	12h15m54s +13h08m57s	13.80	134	SAB(s)b	E	9.09	-21.61	0.84
4222	12h16m22s +13h18m26s	19.73	229	Sc	E	11.57	-19.90	0.67
4244	12h17m29s +37h48m28s	4.35	245	SA(s)cd	E	9.33	-18.86	0.41
4302	12h21m42s +14h35m54s	14.32	1129	Sc	EI	10.06	-20.72	0.74
4395	12h25m48s +33h32m48s	4.76	317	SA(s)m	...	9.55	-18.84	0.34
4429	12h27m26s +11h06m27s	13.00	992	SA(r)0+	...	9.85	-20.72	0.89
4449	12h28m11s +44h05m37s	4.27	203	IBm	...	8.66	-19.49	0.33
4469	12h29m28s +08h45m00s	16.75	582	SB(s)0/a	E	10.85	-20.27	0.86
4517	12h32m45s +00h06m52s	8.39	1127	SA(s)cd	E	9.20	-20.42	0.53
4550	12h35m30s +12h13m15s	15.28	410	SB0	EI	11.52	-19.40	0.78
4551	12h35m37s +12h15m50s	16.06	1200	E2	I	11.79	-19.24	0.90
4565	12h36m20s +25h59m15s	12.07	1226	SA(s)b	E	8.30	-22.11	0.68
4631	12h42m07s +32h32m33s	7.35	615	SB(s)d	EI	7.61	-21.72	0.39
4638	12h42m47s +11h26m32s	17.21	1163	S0-	EI	11.06	-20.12	0.89
4697	12h48m35s -05h48m02s	12.23	1240	E6	...	9.25	-21.19	0.87
4710	12h49m38s +15h09m53s	16.83	1103	SA(r)0+	E	10.71	-20.42	0.77
4754	12h52m17s +11h18m50s	16.02	1317	SB(r)0-	...	10.41	-20.61	0.86
4762	12h52m55s +11h13m51s	10.81	973	SB(r)0	E	10.14	-20.03	0.79
4866	12h59m27s +14h10m15s	29.65	1984	SB(rs)bc	E	10.93	-21.43	0.74
5170	13h29m48s -17h57m59s	29.30	1502	SA(s)c	E	9.85	-22.48	0.72
5576	14h21m03s +03h16m15s	25.20	1422	E3	I	10.80	-21.20	0.85
5577	14h21m13s +03h26m09s	19.23	1489	SA(rs)bc	...	11.66	-19.76	0.75
5713	14h40m11s +00h17m20s	20.32	1948	SAB(rs)bc	...	10.64	-20.90	0.56
5719	14h40m56s +00h19m05s	26.47	1726	SAB(s)ab	...	11.78	-20.32	0.95
5746	14h44m55s +01h57m17s	27.04	1711	SAB(rs)b	E	9.38	-22.78	0.77
5806	15h00m00s +01h53m28s	20.69	1348	SAB(s)b	...	11.16	-20.42	0.60
5811	15h00m27s +01h37m24s	24.17	1523	SB(s)m	...	13.58	-18.34	0.74
5813	15h01m11s +01h42m07s	31.87	1955	E1-2	...	10.36	-22.16	0.92
5814	15h01m21s +01h38m13s	156.31	10526	(R')Sab	...	13.21	-22.77	0.79
5866	15h06m29s +55h45m47s	14.42	674	S0_3	E	9.89	-20.90	0.79
5907	15h15m53s +56h19m44s	17.23	667	SA(s)c	E	9.10	-22.08	0.62
6239	16h50m04s +42h44m23s	24.30	926	SB(s)b	I	11.91	-20.01	0.41
6340	17h10m24s +72h18m15s	19.41	1215	SA(s)0/a	...	10.95	-20.49	0.80
6643	18h19m46s +74h34m06s	20.25	1484	SA(rs)c	...	10.48	-21.05	0.52
6946	20h34m52s +60h09m12s	6.72	45	SAB(rs)cd	...	8.02	-21.12	0.45
7052	21h18m33s +26h26m47s	51.29	4700	E	...	11.72	-21.83	1.71
7217	22h07m52s +31h21m33s	18.28	951	(R)SA(r)ab	...	9.80	-21.51	0.80
7280	22h26m27s +16h08m53s	21.48	1862	SAB(r)0+	...	12.03	-19.64	0.83
7331	22h37m04s +34h24m56s	14.53	815	SA(s)b	...	8.53	-22.28	0.71
7332	22h37m24s +23h47m53s	22.77	1180	S0	E	11.00	-20.78	0.81
7463	23h01m52s +15h58m54s	22.82	2262	SABb	I	12.33	-19.46	0.39
7465	23h02m00s +15h57m53s	27.29	1948	(R')SB(s)0	I	12.40	-19.78	0.64
7479	23h04m56s +12h19m22s	30.20	2380	SB(s)c	...	10.48	-21.92	0.61
7742	23h44m15s +10h46m01s	21.88	1659	SA(r)b	...	11.40	-20.30	0.65
7743	23h44m21s +09h56m02s	18.69	1684	(R)SB(s)0+	...	11.31	-20.05	0.81
UGC4872	09h15m01s +40h02m11s	112.20	8211	SBb	E	13.73	-21.52	0.74
UGC5666	10h28m23s +68h24m43s	4.00	46	SAB(s)m	I	9.69	-18.32	0.33

Table B2. Lists exposure dates, exposure lengths, and the limiting surface brightness level which we reach in our observations.

NGC	Exp.date mm/dd/yy	Exp.length sec x n	SBmin mag/arcsec ²
M49(4472)	13/03/13	300×11	29.3
M51(5194/5195)	21/04/12	300×3	29.9
M59(4621)	24/05/12	300×10	29.1
M60(4649)	13/03/13	300×12	28.6
M63(5055)	29/01/11	300×16	29.5
M65(3623)	12/02/13	300×12	29.1
M66(3627)	13/03/13	300×12	29.6
M74(628)	22/10/11	300×31	29.7
M81(3031)	04/12/11	300×6	29.2
M82(3034)	18/10/12	300×4	28.7
M83(5236)	20/05/12	300×12	28.2
M86(4406)	09/06/13	300×5	28.1
M87(4486)	13/03/13	300×11	29.0
M90(4569)	22/04/14	300×17	28.9
M94(4736)	13/03/13	300×7	28.9
M95(3351)	08/02/11	300×5	28.6
M96(3368)	16/01/13	300×10	29.9
M101(5457)	11/06/13	300×8	29.7
M104(4594)	07/02/13	300×14	29.2
M105(3379)	07/02/13	300×12	29.1
M106(4258)	03/05/11	300×9	27.0
M108(3556)	27/05/14	300×6	28.6
M109(3992)	09/06/13	300×11	28.8
M110(205)	20/10/11	300×8	28.4
125	22/10/11	300×3	28.0
128	22/10/11	300×9	28.1
247	08/10/12	300×9	28.9
278	07/10/16	100×6	28.4
467	16/10/12	300×12	28.0
470	16/10/12	300×12	28.3
474	16/10/12	300×12	28.9
509	19/10/12	300×11	28.6
518	30/11/11	300×4	28.5
520	27/09/16	300×10	28.4
524	30/11/11	300×4	28.3
525	30/11/11	300×4	27.6
530	18/10/12	300×11	28.5
532	30/11/11	300×4	28.2
596	11/12/12	300×11	28.9
636	11/12/12	300×10	29.6
661	19/10/12	300×12	29.1
672	11/12/12	300×13	29.2
720	27/10/11	300×13	29.9
772	18/10/12	300×12	29.0
891	04/09/11	300×11	28.2
925	07/10/16	300×12	28.8
1023	18/10/12	300×6	29.4
1055	20/12/12	300×10	28.3
1084	14/09/12	600×3	28.6
1289	20/11/12	300×9	28.7
1400	10/10/16	300×12	28.4
1407	10/10/16	300×12	28.2
2403	11/12/12	300×13	30.1
2481	16/01/13	300×12	28.4
2549	16/01/13	300×12	28.6
2683	01/01/14	300×12	29.3
2685	30/11/11	300×7	28.3
2768	30/11/11	300×6	28.9
2782	20/11/12	300×7	28.2
2903	20/12/12	300×13	29.4
3032	30/11/11	300×10	28.5

Table B2 – continued

NGC	Exp.date mm/dd/yy	Exp.length sec x n	SBmin mag/arcsec ²
3079	29/03/14	300×196	28.8
3115	20/05/12	300×7	29.4
3156	04/12/11	300×11	28.1
3384	03/05/11	300×18	28.9
3389	03/05/11	300×18	28.6
3521	07/02/13	300×12	29.7
3628	11/12/12	300×11	29.6
4038	24/02/14	300×49	28.5
4096	29/03/14	300×13	29.2
4206	22/04/12	300×11	28.5
4214	22/03/12	300×18	29.1
4216	22/04/12	300×11	29.1
4222	22/04/12	300×11	28.6
4244	14/04/13	300×12	28.9
4302	14/04/15	300×5	28.7
4395	06/06/15	300×17	29.3
4429	13/04/15	300×3	28.8
4449	31/05/11	300×35	28.9
4469	11/04/13	300×14	28.4
4517	29/05/14	300×16	28.5
4550	03/06/14	300×15	28.7
4551	03/06/14	300×15	28.7
4565	14/05/12	300×18	30.0
4631	14/04/13	300×12	29.8
4638	24/05/12	300×10	29.1
4697	22/02/15	300×2	29.1
4710	11/04/13	300×15	28.6
4754	18/05/12	300×7	28.1
4762	18/05/12	300×7	28.9
4866	12/02/13	300×12	29.2
5170	25/02/14	300×22	29.5
5576	20/04/12	300×21	29.4
5577	20/04/12	300×21	28.2
5713	03/06/11	300×10	28.5
5719	03/06/11	300×10	28.3
5746	20/05/12	300×9	28.9
5806	11/04/13	300×10	28.5
5811	11/04/13	300×10	28.2
5813	11/04/13	300×10	28.4
5814	11/04/13	300×10	28.4
5866	20/05/12	300×7	29.0
5907	09/06/13	300×13	29.0
6239	08/10/12	300×4	28.4
6340	11/06/13	300×9	28.1
6643	20/05/12	300×5	28.0
6946	21/09/11	300×14	28.4
7052	06/09/16	300×6	28.5
7217	29/08/16	300×12	28.6
7280	19/10/12	300×8	28.6
7331	21/08/12	600×8	28.4
7332	11/06/13	300×8	28.1
7463	14/09/12	600×6	28.1
7465	14/09/12	600×6	27.7
7479	17/09/12	600×6	28.8
7742	14/09/12	600×7	29.2
7743	14/09/12	600×7	28.3
UGC4872	16/10/12	300×9	26.9
UGC5666	16/01/13	300×12	28.7

Table B3. Lists our envelope diameter measurements (at the 28 mag/arcsec² isophote) for each galaxy in arc-minutes and kpc, along with the envelope shape for each envelope.

NGC	Diameter arcmin	Diameter kpc	Envelope shape
M49(4472)	41.5 ± 1.7	200.8 ± 8.4	Round
M51(5194/5195)	26.8 ± 0.9	66.8 ± 2.1	Disturbed
M59(4621)	17.0 ± 0.9	72.9 ± 3.9	Round
M60(4649)	14.6 ± 0.5	72.6 ± 2.5	Round
M63(5055)	38.1 ± 1.2	100.2 ± 3.0	Oval
M65(3623)	12.0 ± 0.2	44.9 ± 0.9	Slightly boxy
M66(3627)	22.4 ± 0.5	74.8 ± 1.6	Oval
M74(628)	13.9 ± 0.1	40.9 ± 0.3	Round
M81(3031)	33.6 ± 0.8	35.2 ± 0.8	Oval
M82(3034)	41.3 ± 1.6	43.5 ± 1.7	Slightly oval
M83(5236)	22.9 ± 0.5	32.7 ± 0.7	Round
M86(4406)	25.8 ± 1.1	130.4 ± 5.5	Round
M87(4486)	41.8 ± 2.4	204.0 ± 11.5	Oval
M90(4569)	16.7 ± 0.7	57.7 ± 2.4	Oval
M94(4736)	23.5 ± 0.3	30.0 ± 0.4	Round
M95(3351)	11.7 ± 0.6	33.8 ± 1.7	Oval
M96(3368)	14.2 ± 0.1	40.4 ± 0.2	Oval
M101(5457)	32.7 ± 0.6	67.6 ± 1.2	Round
M104(4594)	30.8 ± 1.2	77.0 ± 3.0	Round
M105(3379)	19.5 ± 0.7	64.1 ± 2.4	Round
M106(4258)	—	—	Slightly diamond
M108(3556)	22.3 ± 0.5	63.6 ± 1.3	Oval
M109(3992)	10.7 ± 0.4	79.0 ± 2.6	Oval
M110(205)	36.0 ± 2.3	8.4 ± 0.5	Slight parallelogram
125	3.6 ± 0.3	66.3 ± 6.2	Circular
128	7.6 ± 0.7	99.6 ± 9.3	Oval
247	28.3 ± 0.7	30.5 ± 0.8	Disky
278	7.0 ± 0.3	36.1 ± 1.4	Circular
467	6.8 ± 0.2	116.3 ± 3.1	Circular disturbed
470	4.2 ± 0.2	59.3 ± 2.9	Oval
474	7.9 ± 0.6	62.9 ± 5.0	Circular disturbed
509	2.3 ± 0.1	21.8 ± 1.2	Oval
518	3.4 ± 0.2	38.6 ± 1.8	Oval
520	6.0 ± 0.2	31.0 ± 0.8	Disturbed
524	13.7 ± 0.4	129.6 ± 3.7	Circular
525	—	—	Diamond
530	2.0 ± 0.1	41.8 ± 2.4	Oval
532	8.0 ± 0.4	80.2 ± 4.0	Oval
596	15.7 ± 0.7	98.2 ± 4.1	Circular
636	9.2 ± 0.4	79.1 ± 3.3	Circular
661	5.9 ± 0.3	64.0 ± 3.2	Round
672	10.2 ± 0.5	21.4 ± 1.0	Oval
720	19.7 ± 0.9	156.8 ± 6.8	Boxy
772	14.8 ± 0.7	109.9 ± 5.2	Oval disturbed
891	13.1 ± 0.2	37.4 ± 0.6	Diamond
925	12.3 ± 0.3	32.8 ± 0.8	Oval
1023	18.0 ± 0.5	50.1 ± 1.4	Boxy hexagon
1055	20.2 ± 0.9	113.4 ± 5.0	Boxy hexagon
1084	12.1 ± 0.7	54.3 ± 3.3	Round
1289	6.4 ± 0.5	56.0 ± 4.4	Round
1400	10.1 ± 0.7	76.9 ± 5.0	Round
1407	17.6 ± 1.0	146.0 ± 8.6	Round
2403	26.4 ± 0.5	24.6 ± 0.5	Oval
2481	3.2 ± 0.1	29.1 ± 1.1	Oval
2549	6.2 ± 0.1	22.5 ± 0.3	Oval
2683	11.4 ± 0.4	31.2 ± 1.0	Diamond
2685	7.1 ± 0.3	26.1 ± 1.1	Slightly diamond
2768	14.9 ± 0.5	95.8 ± 3.5	Round
2782	7.3 ± 0.2	36.3 ± 1.2	Round disturbed
2903	24.1 ± 0.6	65.3 ± 1.7	Disky
3032	4.3 ± 0.2	24.8 ± 1.0	Round

Table B3 – continued

NGC	Diameter arcmin	Diameter kpc	Envelope shape
3079	11.2 ± 0.5	53.8 ± 2.2	Oval
3115	24.8 ± 1.0	69.7 ± 2.9	Oval
3156	5.0 ± 0.3	32.2 ± 1.8	Oval
3384	12.3 ± 0.1	33.8 ± 0.2	Oval
3389	4.7 ± 0.1	26.6 ± 0.8	Oval
3521	22.4 ± 0.4	80.6 ± 1.4	Oval/diamond
3628	20.7 ± 0.2	65.1 ± 0.5	Boxy
4038	16.1 ± 1.6	114.7 ± 11.6	Disturbed with antennae
4096	13.1 ± 0.3	45.7 ± 1.1	Disky
4206	6.8 ± 0.2	37.3 ± 1.0	Oval
4214	11.6 ± 0.2	10.0 ± 0.1	Round
4216	10.7 ± 0.1	42.8 ± 0.3	Boxy
4222	6.9 ± 0.3	39.8 ± 1.6	Disky
4244	22.1 ± 0.5	27.9 ± 0.7	Disky
4302	11.0 ± 0.2	45.8 ± 0.9	Oval
4395	16.9 ± 0.3	23.4 ± 0.4	Round
4429	12.1 ± 0.4	45.8 ± 1.4	Oval
4449	21.3 ± 0.7	26.4 ± 0.9	Round
4469	10.8 ± 0.5	52.8 ± 2.2	Oval
4517	18.5 ± 0.9	45.1 ± 2.1	Oval
4550	6.3 ± 0.3	27.8 ± 1.3	Diamond
4551	4.5 ± 0.3	21.2 ± 1.2	Round
4565	21.1 ± 0.6	74.1 ± 2.1	Diamond
4631	21.5 ± 0.4	46.0 ± 0.9	Boxy
4638	5.3 ± 0.3	26.7 ± 1.7	Round
4697	17.5 ± 0.7	62.1 ± 2.6	Round
4710	9.4 ± 0.4	46.0 ± 1.9	Diamond
4754	7.9 ± 0.6	36.7 ± 2.7	Oval
4762	14.9 ± 0.4	47.0 ± 1.2	Boxy
4866	8.0 ± 0.2	68.8 ± 1.8	Oval
5170	11.6 ± 0.2	98.7 ± 1.6	Boxy/diamond
5576	11.5 ± 0.4	84.0 ± 2.8	Round
5577	4.4 ± 0.2	24.9 ± 0.9	Disky
5713	4.8 ± 0.1	28.2 ± 0.8	Round
5719	7.0 ± 0.2	53.7 ± 1.6	Slightly diamond
5746	11.1 ± 0.4	87.0 ± 3.2	Oval
5806	7.3 ± 0.2	43.6 ± 1.2	Oval
5811	3.2 ± 0.1	22.7 ± 0.5	Oval
5813	16.5 ± 0.7	153.1 ± 6.5	Oval
5814	6.7 ± 0.4	305.8 ± 17.2	Oval
5866	9.1 ± 0.3	38.4 ± 1.1	Round/boxy
5907	15.5 ± 0.3	77.9 ± 1.7	Oval
6239	5.3 ± 0.3	37.6 ± 1.9	Disturbed
6340	11.5 ± 0.8	65.1 ± 4.4	Round
6643	5.5 ± 0.2	32.4 ± 1.4	Oval
6946	25.9 ± 0.5	50.7 ± 1.0	Round
7052	7.8 ± 0.4	116.2 ± 6.2	Boxy
7217	11.0 ± 0.4	58.5 ± 1.9	Round
7280	3.4 ± 0.1	21.3 ± 0.8	Round
7331	14.7 ± 0.5	62.3 ± 1.9	Diamond
7332	5.2 ± 0.1	34.3 ± 1.0	Diamond
7463	6.4 ± 0.3	42.8 ± 1.9	Disturbed
7465	—	—	Round
7479	8.2 ± 0.4	71.8 ± 3.1	Oval
7742	4.7 ± 0.1	29.9 ± 0.6	Round
7743	8.5 ± 0.4	46.4 ± 2.0	Oval
UGC4872	—	—	Oval
UGC5666	16.7 ± 0.6	19.4 ± 0.7	Oval